EFFECT OF SMALL CERIUM ADDITIONS ON MICROSTRUCTURE AND MECHANICAL PROPERTIES OF AL-MG-FE ALLOY

By

XIAOFEI YAN, B.Eng.

A Thesis

Submitted to the School of Graduate Studies

In Partial Fulfillment of the Requirements

For the Degree of

Master of Applied Science

McMaster University

MASTER OF APPLIED SCIENCE (2007) McMaster University

(Materials Science and Engineering) Hamilton, Ontario

TITLE: Effect of Small Cerium Additions on Microstructure and Mechanical Properties of Al-Mg-Fe Alloy

AUTHOR: Xiaofei Yan, B.Eng. (Shanghai Jiao Tong University)

SUPERVISOR: Professor David S. Wilkinson and Dr. Dmitri V. Malakhov

NUMBER OF PAGES: xii, 116

ABSTRACT

The application aluminum sheet alloy for light vehicle development was limited by the high cost of alloy fabrication. The impurity iron, which is easily picked up during fabrication, deteriorates its formability. The sheet alloy produced by continuous casting techniques was showing lower in-service performance than the one produced with traditional high-cost direct-chill casting technique. Therefore, enhancing the general formability of the aluminum alloy became the aim of many researchers and engineers in past decades.

This project was launched to detect a possible modification effect of rare-earth (RE) element on a Al-Mg-Fe alloy, which is a simplified AA5754 alloy. Cerium was chosen as the RE element to test with. The influence of this rare-earth element on the alloy grain microstructure, phase morphology, and corresponding mechanical behavior was investigated.

It was found that cerium had a modification effect on the phase morphology to some extent. Its addition provided a great grain refinement in as-cast alloys. However, after thermo-mechanical processing, this effect would be eliminated by the small broken particles and recrystallized fine grains. It was found that the mechanical performance of

the cerium-containing AA5754 was neither enhanced nor deteriorated. The AA5754 alloy remained non-heat-treatable after the addition of cerium.

ACKNOWLEDGEMENTS

I would like to first express my sincere gratitude to Professor David S. Wilkinson and Dr. Dmitri V. Malakhov for their invaluable guidance over the last two years. Their careful co-supervision and patience in research discussion provided me great opportunities to develop personal problem solving ability and critical thinking when facing challenging. I also want to thank Professor Sumanth Shankar for his technical support.

Many thanks to Mr. Pierre Marois and Dr. Mark Gallerneault from Novelis for the research experience and experimental support provided to this project. I also want to express my appreciation to Professor Hani Henein, Dr. David Mitlin and Dr. Jian Chen from University of Alberta for a fruitful collaboration.

The people in the MSE department made my two years in McMaster full of joy and wonderful memories. The amazing people I met here helped me to discover the Canadian culture and made my stay in Ontario a rich story. I also want to give my thankfulness to certain people: Mehdi Hosseinifar for his generous help at the beginning of the research and Sandy Wu for her encouragement during difficulties. Finally, I want

to thank to my family, especially my mother Fei CHEN and my father Xingbo YAN, for their unconditional supporting all the time.

Last not least, I am grateful to Auto 21 for the financial support to this project.

TABLE OF CONTENTS

LIST OF FIGURES

LIST OF TABLES

1 INTRODUCTION AND OBJECTIVES

The mass of aluminum alloys contained in each new vehicle has increased significantly during the past decade. Because of a combination of high strength, good formability and low density, aluminum alloys have received much attention for fuel-efficient vehicle development. Moreover, recyclability of aluminum alloys helps environmental protection and reduces the production cost. However, this cost is still 4 to 5 times of that of the steel, and hence limits aluminum alloy application for light vehicles.

The Direct-Chill (DC) casting technology traditionally used to produce Al billets contributed to the high production price in terms of time, labor, energy and capital. In particular, extensive thermo-mechanical processing must be applied to turn the cast ingot (typically 300-500 mm in thickness) into the final aluminum sheet with gauge thickness of 1-2mm. The Al industry has developed continuous casting (CC) as an alternative process. The molten metal is cast directly into slab about 10mm thick. This continuous casting eliminates several processing steps and hence results in significant savings for the aluminum sheet alloy production.

However, the lower-cost CC alloy seemed not to attain the same formability as the DC cast alloy. It was shown by Kang *et al.* (2006) that the CC AA5754 alloy shows lower

fracture strain than the DC cast AA5754 alloy. This seems to be related to the nature of the constituent particles and the differences in spatial distributions in these alloys. In CC alloys, higher fraction of particles forms in stringers, where the particle interspacing is significantly reduced. It seems that modification of these intermetallics may be a key to improving the alloy performance.

One problem related to the recycling of aluminum alloys is an accumulation of iron. Iron is detrimental to the formability of the AA5754 alloy (Sarkar *et al.*, 2001). Because of a low solubility in the aluminum matrix, iron precipitates to form brittle and acicular intermetallic particles. The amount of these Fe-rich particles would increase several times when such alloys are recycled. A lot of "neutralizer" or "modifier", e.g. Sr, Ti (Suarez-Pena *et al.*, 2006) have been added to various aluminum alloys to test their effects on the Fe-rich particles. Many of these neutralizers or modifiers formed their own aluminides, and also changed the volume fraction and morphology of the Fe-rich particles to varying degrees (Khudokormov *et al.*, 1975, Asensio-Lozano *et al.*, 2006, Chen *et al.*, 2006). The majority of their modification effect came from the grain refinement and second-phase constituent particle modification (Ravi *et al.*, 2001). However, no results indicated the formation of phases improving the alloy formability.

A slight composition variation of a wrought aluminum alloy can lead to perceptible difference of alloy microstructure and mechanical property. Since the majority of metals, except Mg and Cu, have a very low solubility in solid aluminum, alloying elements would be continually rejected from the growing FCC aluminum dendrites, and accumulate in the remaining melt and form interdendritic substance at the very last stage of solidification. Attributed to the variant nature of the intermetallic phases in the aluminum alloy, which have similar Gibbs energies of formation (per formula unit), many new second phase constituents appear if the overall composition alter a little. These newly-appeared intermetallic particles have different particle size, aspect ratio and spatial distribution. They changed the microstructure significantly and hence influence the alloy mechanical behavior. Therefore, it can be hoped to improve the alloy performance by small additions of chemical elements.

It is hoped that by coupling thermodynamics with the Scheil formalism, the phase assembly in the as-cast alloys can be predicted for any alloy composition. However, due to lack of reliable thermodynamic properties of these intermetallic phases, and the complexity of an actual solidification process, it is difficult to predict what phases would precipitate. Besides, a precipitation sequence depends on cooling rate. Some of these phases are not even seen on the equilibrium phase diagrams. Thermo-mechanical

processing also changes the overall alloy microstructure and mechanical properties. Therefore, besides the theoretical study of phase formation with thermodynamics, a laborious experimental investigation of the as-cast and thermo-mechanical processed microstructures of different composition alloys is necessary.

The majority of intermetallics observed in AA5754 are iron-contained, which are generally brittle needles or rods that deteriorate alloy ductility and bendability. To diminish a portion of these acicular phases or to transfer them into a more globular shape, a modifier can be employed into the alloy.

It is accepted through experimental trials that individual rare-earth element has better modification ability than mischmetal. Some preliminary investigations indicated that the lanthanides showed different effect on aluminum alloys, and it was mentioned that this difference might be related to their diverse atomic radii, typical valence and affinity to other chemical elements (Sun, 1992). Since the mechanism behind the reaction of rare earth element with other alloying elements is unknown, it would take many years of dedicated effort and generous funding to thoroughly investigate with each rare-earth element.

Sr is powerful in microstructure modification by inhibiting the formation of a detrimental β-Al_5FeSi phase in Al-Si-Fe alloys. It is believed that at early stages of solidification, the Chinese script of α-Al_8Fe_2Si phase precipitates first and then reacts with the remaining liquid to form the acicular β (Mula. 1996):

$$L + Al_8Fe_2Si \rightarrow L + Al + Al_5FeSi$$

The early-precipitated α phase particles are shielded from the melt by the absorption of Sr atoms, thus the reaction mentioned above is suppressed. Therefore, the formation of acicular β is reduced while more of the less detrimental α appeared. It was reported that only 0.04-0.06% of Sr was sufficient to introduce an enormous microstructural difference. Nothing was mentioned about why and how Sr was chosen. Therefore, it should be realized this discovery exemplifies the fact that sometimes important or useful findings comes from trials and errors, and the Edisonian approach worth trying when only limited information is available.

In this research, it was decided to use Ce to explore its modification effect on the microstructure of AA5754 aluminum alloy, and see what changes a small addition of this metal bring to the alloy formability and microstructure.

During the last century, there were disputable and contradictive findings about the

influence of cerium addition on aluminum alloys. The effect of cerium has been recorded in various alloys (Salazar *et al.*, 2002, Ravi, *et al.*, 2002). However, there is no record about Al-Mg-Fe alloy yet. In addition, a series of experiments with mischmetal conducted at Alcan several years ago, which was mentioned during a private communication by Dr. Lloyd, indicated that the results were promising although the details cannot be publicly disclosed. Therefore, it is worth investigating what effect additions of cerium could be on the formability of Al-Mg-Fe alloy, especially what phase formed in the Al matrix.

The price of cerium is relatively acceptable compared to the other pure rare-earth metals. Considering the production cost, only small additions of cerium, less than 0.5%, are applied to Al-Mg-Fe alloy modification.

The fabrication of sheet alloy involves thermo-mechanical processing. This procedure is extensive and complex for DC comparing to that of a CC alloy. Since the aim of this research is to improve the formability of both the DC and CC alloys, the effect of small cerium addition on AA5754 alloy was investigated on a series of as-cast and thermo-mechanical processed alloys.

Even though the result eventually may not be as expected, a systematic

investigation of the microstructure and mechanical properties of Ce-doped Al-Mg-Fe alloys in various tempers will be of merit, and will assist the study on other rare-earth elements in the long run.

2 LITERATURE REVIEW

2.1 AA5754 Alloy

2.1.1 The Strengthening Mechanisms of AA5754

AA5754 is a typical Al-Mg alloy with a magnesium content level in the range of 2.6-3.6 wt.% (as seen in Table 2.1) . The solubility of magnesium in aluminum varies from 17.4wt.% to 1.7 wt.% , along the solvus of Al-Mg phase diagram (as seen in Figure 2.1. This big decrease in solubility provides a necessary condition for the formation of a supersaturated solid solution in the Al-Mg alloy. Due to the difficulty for magnesium to precipitate out from the Al matrix, this supersaturated solid solution decomposes very slowly such that it can be retained in solution through the thermo-mechanical processing and kept for a very long time.

Table 2.1 Typical alloy elements of AA5754 (Metals handbook Vol. 2)

Alloy Elements	Si	Fe	Mn	Mg
Composition (wt. %)	≤0.4	≤0.4	≤0.5	2.6-3.6

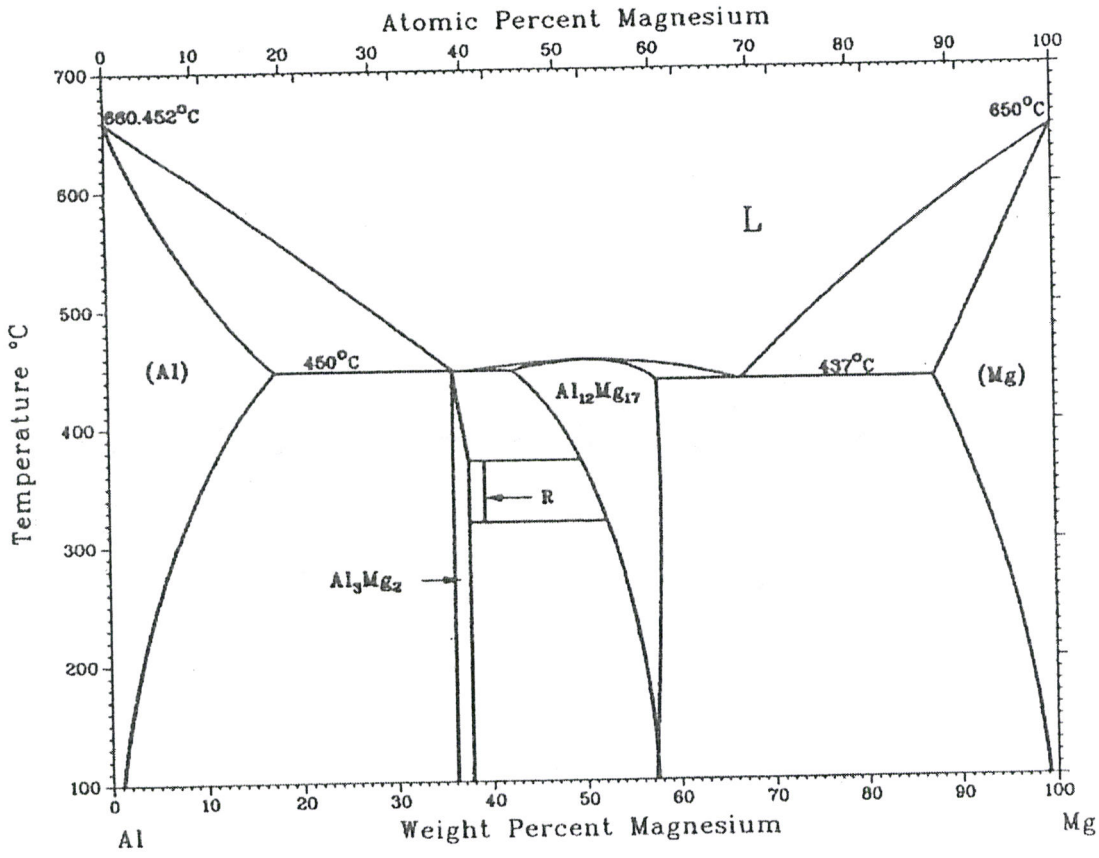

Figure 2.1 Al-Mg phase Diagram (ASM Handbook Vol.3)

Al-Mg alloy (5xxx series), ranging from 0.5 to 6 wt.% Mg, is well known as a solute strengthened work hardening alloy (Morris *et al.*, 2002). Its high strength is gained through mechanical working. During the deformation and intermediate annealing, the magnesium atoms, which can play the role of solute drag in the Al matrix, restrict the movement of dislocations and grain boundaries as they pass, and hence retain a relatively high lattice strain for the alloy (Dieter, 1986). Therefore, the deformed structure as well as the strength is partially kept by the magnesium atoms. The

constituent particles also inhibit the migration of dislocations and grain boundaries, but their effect is not as obvious as that due to the highly concentrated Mg atoms. Therefore, the strengthening effect is achieved and attained by the combination of the working and solute dragging.

Manganese is added with combined purposes of solid solution strengthening and grain refinement. With a very low solubility in aluminum matrix, most of the manganese is precipitated in the form of dispersoids with Al, Fe, Mn and Si, e.g. $Al_6(Fe,Mn)$, $Al_{12}(Fe,Mn)_3Si$ during the ingot reheating (Li *et al.*,2004, Griger *et al.*,1996). These finely distributed dispersoids enhance the material strength.

2.1.2 The Non-Heat-Treatable Alloy

The way to define a non-heat-treatable alloy is to see whether there is significant strength and hardness increase of the material after an artificial aging. In other words, if there is precipitation hardening in this alloy, it is heat-treatable, e.g. Al-Cu alloys. Otherwise, it is non-heat-treatable, e.g. AA5754 alloy.

In as-cast Al-Mg-Fe alloy, because of the low solubility of alloy elements in the α-Al matrix, most of the second phase constituents formed between the dendrite arms or

along the grain boundaries. The most common phases of particles formed in cast AA5754 are specified as in Table 2.2.

Table 2.2 Characteristics of intermetallic phase in AA5754 alloys (ASM Vol.9)

Phase	Chemical Composition		Morphology of Precipitates
	wt.%	at.%	
α-Al	100	100	Matrix, dendrites
$Al_{13}Fe_4$	40.8%Fe	25%Fe	Needles or rosettes
Al_6Fe	25.65% Fe	14.3%Fe	Platelets or rods
β-Al_3Mg_2	34.8-37.1%Mg	40%Mg	Compact, rounded particles
Al_6(Mn, Fe)	25.34%Mn	14.3%Mn	More or less elongated
Mg_2Si	63.2%Mg, 36.8%Si	66.6%Mg, 33.3% Si	Fine Chinese script, dispersed particles
α-AlFeSi	30-33%Fe, 6-12%Si	9.1%Si, 18.2%Fe	Chinese script

These constituents are dominated by the iron-rich phases, which mainly consist of the stable phase $Al_{13}Fe_4$ and the metastable phases Al_6Fe, Al_mFe (m=4.0-4.4) (Liang *et al.*, 1993). Ternary phases containing Al, Fe, Mn and Si are also present. The morphologies of Fe-rich particles are mostly needles or platelets, but some of them form as Chinese script in the cast AA5754 alloy, as seen in Figure 2.2. These Fe-rich particles precipitate at high temperature or even form in the liquid phase, and do not dissolve in Al matrix during later heatings (ASM Handbook Vol.2). There is no huge amount of small particles precipitate during low temperature heating and the AA5754 is a non-heat-treatable. The negligible presence of Mg_2Si in AA5754 alloy is not sufficient to generate the extensive

precipitation hardening that appears in 6xxx alloy.

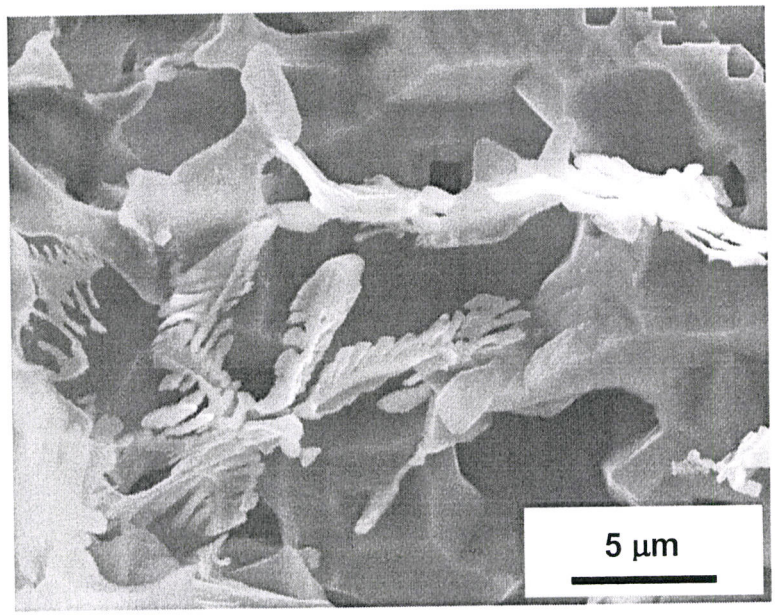

Figure 2.2 The SEM picture of deep-etch-revealed iron-rich particle in AA5754 alloy (Azari *et al.*, 2004)

2.2 The Effect of Iron Content on the Formability of AA5754

Iron is impurity in commercial aluminum and its alloys. It is easily picked up from tools and machines during practical production, which results in a much higher concentration if the material is recycled. Therefore, in high Fe alloy, there would be more acicular intermetallic particles formed, which is detrimental to the formability of the alloy.

2.2.1 Effect of Iron Content on the Fracture Mechanism of AA5754 Sheet Alloy

The traditional damage accumulation process observed in ductile commercial materials is dominated by the steps of void nucleation, growth and coalescence. These voids are generated around the second phase particles themselves and linked up by the plastic flow. Eventually a cup and cone fracture is developed by these voids and cracks (Brown *et al.*, 1983).

In AA5754, little damage was observed prior to fracture (Lloyd, 1980). The evolution of failure involve with shear localization (Teirlinck et al., 2000). Korbel *et al.* (2004) indicated that, in Al-Mg alloys, shear localization occurred due to the dynamic recovery in the aluminum matrix. Such recovery was caused by the diffusion of unpinned dislocation. It would lead to local softening and the formation of shear bands. It was proposed by Spencer *et al.* (2001) that, in the alloys with high volume fraction of particles, the spacing between voids was much decreased. Damage developed along the shear bands would immediately lead to an fracture because lower strains are required for the void linkage. Therefore, in AA5754 alloy, the failure mechanism was a result of the competition between shear localization and void initiation, growth and coalescence.

Spencer *et al.* (2001) concluded that the shear localization dominated in the

low-iron AA5754 alloy and was responsible for the higher alloy ductility. In high-iron AA5754 alloy, once the damage was initiated, its coalescence and linking up process was more responsible for the failure of this alloy and resulted in a lower ductility.

2.2.2 Effect of Iron Content on the Ductility and Bendability of AA5754 Sheet Alloy

Sarkar *et al.* (2001) observed that, when increasing the iron content from 0.08 wt.% to 0.3wt. %, the alloy ductility decreased and the fracture mode transformed from cup and cone type to void sheeting type (as seen in Figure 2.3). The low Fe alloy had a better bendability than the high Fe alloy, and the surface imperfection varied from small undulations to obvious cracks on the specimen surface during the bend test (as seen in Figure 2.4).The pre-strain had much more influence on the high Fe alloy. Due to the high volume fraction of particles, the shear localization and damage initiation caused by pre-strain were much more severe than that in the low-iron alloy. When alloys were further pre-strained, the ductility and bendability of the high-iron alloy decreased a lot while that of the low-iron alloy had no significant changes.

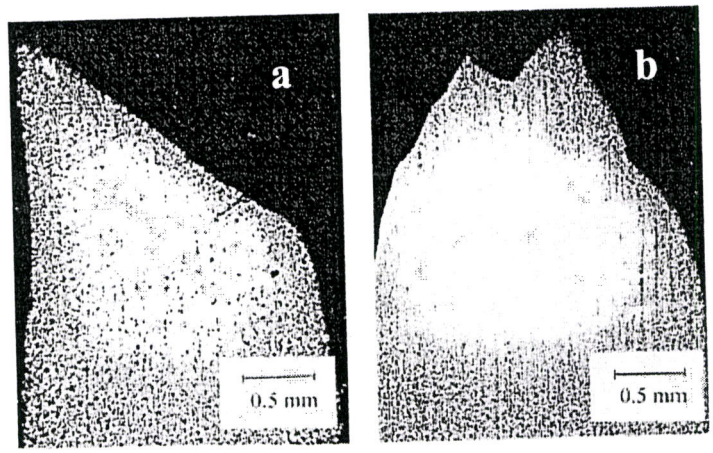

Figure 2.3 The fractures of (a) 0.3wt. % Fe alloy (b) 0.08 wt. % Fe alloy tension specimens (Sarkar *et al.*, 2001)

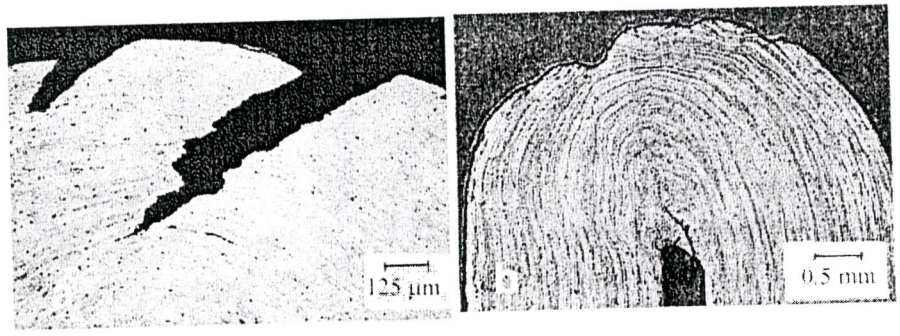

Figure 2.4 (a) Cracking in high Fe alloy (b) undulation in low Fe alloy (Sarkar *et al.*, 2001)

Alloy bendability was defined as the ratio of r_{min}/t, where r_{min} was the minimum bend radius and t was sheet thickness. The bendability of a material could be related to its ductility through an empirical equation $\frac{r_{min}}{t} = \left(\frac{C}{RA} - 1\right)$ proposed by Datsko and Yang (1960), where RA was the reduction percentage in area in a tensile test, and C was a constant standing for a reduction in area percentage. If the RA exceeded the C, the

bendability of the material would be zero. Because the alloy's RA in a tensile test is much easier to be measured than the r_{min}/t of a bending test, therefore, it is possible to use present RA results of different alloys to predict their bendability relations.

2.3 Effect of Continuous Casting Technology on AA5754 Sheet Alloys

In the report by Kang *et al.* (2006), the strip cast (CC) alloy shows a lower tensile fracture strain than the DC cast alloy. The compositions of the DC alloy and CC alloy studied by Kang were as seen in Table 2.3. It turned out that more fractions of particles formed in stringers in the CC alloy and more of these stringers were associated with Mg_2Si particles. It was the stringer that led to the different damage process in the CC AA5754 alloys.

Table 2.3 Chemical composition of CC and DC AA5754 sheet alloys (in wt. %) (Kang *et al.*, 2007)

	Mg	Mn	Si	Fe	Al
CC	3.50	0.21	0.11	0.21	Bal.
DC	3.11	0.25	0.06	0.21	Bal.

The interspacing of particles in stringers was much smaller than those for isolated particles. This difference of particle special distribution is related to the cooling rate,

which is much faster of CC alloy than that of DC alloy. The dendrite spacing in CC alloy is therefore smaller than that in as-cast DC alloy. Since the intermetallics accumulated between the dendrite arms, the smaller the dendrite arm spacing is, the more stringers of particles will form. The strains for initiating damage around stringers would be much lower than those for the isolated particles. Therefore, with a higher volume fraction of stringers, the strain leading to final fracture in the CC alloy would be much lower than that in the DC alloys. Accordingly, the failure mode transferred from a cup and cone type to a shearing type, as observed as in Figure 2.5.

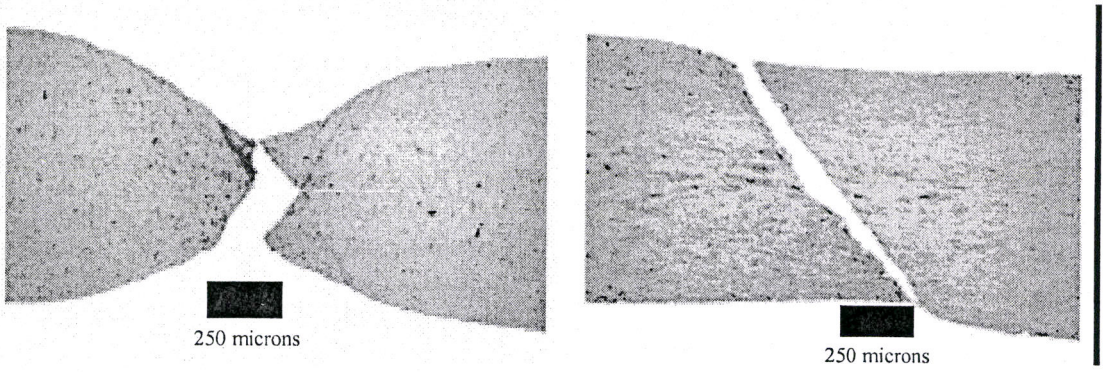

Figure 2.5 Shear banding and tensile fracture of DC (left) and CC (right) AA5754 cast alloys (Kang *et al.*, 2007).

2.4. Modification Effect of Chemical Additions on Aluminum Alloys

The presence of the brittle and acicular intermetallics distributed through the Al matrix causes damage and premature failure in the variant sheet forming operations. If

this problem could be solved by small additions of metals, which would modify those brittle angular intermetallics to small fine particles, the initiation of damage could be delayed and the formability of alloys would be enhanced both for the DC and CC alloys.

Rare-earth (RE) elements have been studied for improving the microstructure and mechanical properties of aluminum alloys. Mischmetal consists of about 50 at.% Cerium, 27 at.% La, 5 at% Pr, 16 at.% Nd and 4 at.% other RE metals (REM) (Saccone *et al.*, 1997). These rare-earth elements are lanthanides in the periodic table. As illustrated in Table 2.4, their electronegativities and atomic radius are close, which indicate their similar physical and chemical behaviors. It was found that some pure RE elemental additions had better modification ability than the mischmetal (Sun, 1992). However, from La to Er, their modification effect on as-cast Al-Si alloys varied a lot. Sun (1992) proposed that, if arranging them in the order of modification ability, Er would top the list while Ce attains a medium place. The mechanism for this was still unclear. Due to that the pure Ce has a relatively acceptable price, many trials had been done with it on various aluminum alloys.

Table 2.4 Comparison of physical properties of certain RE elements and aluminum (ASM Handbook, Vol.2)

Property \ Element	La	Ce	Pr	Nd	Er	Al
Atomic number	57	58	59	60	68	13
Electronegativity (Scale Pauling)	1.10	1.12	1.13	1.14	1.24	1.61
Atomic radius(pm)	195	185	185	185	175	125

2.4.1 Early Studies of Effect of Cerium on Pure Aluminum and Aluminum Alloy

Barth (1912) found out that a small addition of cerium increased the strength and ductility of aluminum which contained impurities of iron and silicon. Based on his chemical composition analysis, he postulated that cerium removed silicon by forming cerium silicide. This cerium silicide would act in the similar way as Mg_2Si and provide age hardening to the alloy. However, he did not attribute the improvement in ductility as much to the removal of silicon as to the removal of porosity, the explanation for which was not given. Schulte (1921), who later repeated this work on pure Al, Al-Cu and Al-Mg alloys, also observed an increase in ductility among the cerium-containing alloys. Instead of silicon, he found that, after addition of cerium, the amount of nitrogen in the alloys decreased. The addition of cerium aided of the elimination of aluminum nitride, hence enhanced the alloy ductility.

Gillett and Schnee (1923) threw doubt on these previous conclusions with their different results on Al-4 wt. %Cu alloys. The addition of cerium did not provide any hardening effect on the alloy after heat treatment, and no silicide was observed in the microstructure. Gillett and Schnee alleged that the increase of ductility in Schulte's work was possibly a data variation from sample to sample. But they admitted that since the addition of cerium-group metals contained iron, an extra amount of iron would decrease the ductility of the alloys. It was possible that the pure cerium enhanced the ductility of aluminum alloys, but the improvement was not revealed because iron was added as well.

2.4.2 Effect of Cerium on the Cast Al-Si-Mg Alloys

Al-Si-Mg alloys also have wide applications in the automotive industry. Similar to AA5754 alloy, iron formed the brittle intermetallics with other alloying elements. These intermetallics could be $\alpha(Fe_2SiAl_8)$, $\beta(FeSiAl_5)$, and $\pi(FeMg_3Si_6Al_8)$ and others. Among them, the needle-shape β phase was associated with the deterioration of mechanical properties (Ravi *et al.*, 2002). Due to its acicular morphology, it would result in stress concentration around itself and hence lead to damage nucleation, as seen in Figure 2.6.

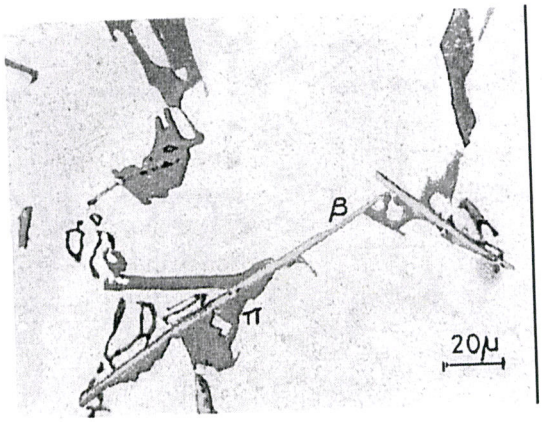

Figure 2.6 The morphologies of β($FeSiAl_5$), and π($FeMg_3Si_6Al_8$) in AC Al-Si-0.6 wt. %Fe alloy (Ravi *et al.*, 2002).

But with a small addition of a "neutralizer" like a RE element, the harm of the β needles to the aluminum alloys could be decreased by reducing the volume fraction of this phase and modifying its morphology. It was observed that rod-like Al-Ce and Al-Ce-Fe-Si intermetallics compounds formed in the cerium added alloy. These particles had a finer size. By consuming Al, Fe and Si, they inhibited the formation of β phase by reducing its size and volume fraction (as seen in Figure 2.7). These finer intermetallic compounds hence improved the strength and ductility of the alloy. It was also observed that the grain structure was refined as well, which further enhanced the mechanical properties of the alloys (Ravi *et al.*, 2002).

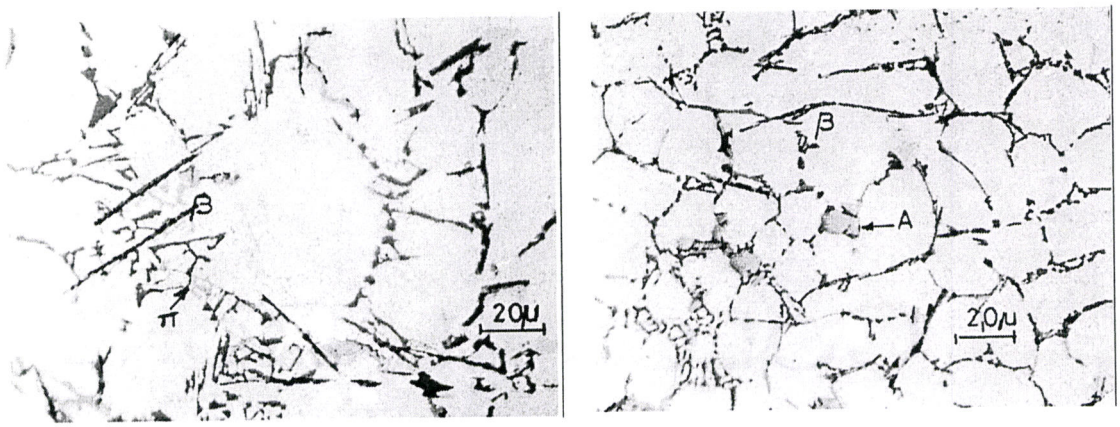

Figure 2.7 Microstructures of Al-Si-0.6wt.% Fe as-cast alloy(Left) and Al-Si-0.6wt.% Fe-1wt.% mischmetal. β-($FeSiAl_5$); A- cerium-rich particle.(RAVI *et al.*, 2002)

Li *et al.* (2006) also reported that 1 wt.% addition of cerium to the eutectic and hypereutectic Al-Si alloys not only modified the needle shape eutectic Si into finer ones but also refined the α-Al by reducing the dendrite arm spacing.

Therefore, the addition of cerium to Al-Si-Mg improved both its strength and ductility by forming finer intermetallic particles and refining alloy microstructures.

2.4.3 Effect of Erbium on Aluminum Alloy

Xu *et al.* (2006) studied the effect of additions of erbium on the microstructure and tensile behavior of Al-5 wt. % Mg alloys. They found that erbium reduced the dendrite arm spacing of the cast alloys and had a great refinement effect on grain structure. The strength of the alloys increased as a result of the Er additions. Up to 0.4 wt. %, both the strengths of the cold-rolled and annealed alloys were enhanced When more

Er was added, no more obvious strength enhancement was observed but the material ductility deteriorated.

Because of a low solubility of Er in solid Al, most of it precipitated as Al_3Er intermetallic compound in the grains and these spheroids were named primary Al_3Er (Tang *et al.* 1992). It was because a secondary Al_3Er would later precipitate from the supersaturated solid solution and spread around the microstructure as fine dispersoids. The primary Al_3Er acted as cites of the heterogeneous nucleation and hence refined the grain microstructure. The secondary Al_3Er finely distributed across the microstructure and effectively retarded the migrations of dislocations and grain boundaries and hence enhanced the alloy strength. The strengthening mechanism in this alloy is a combination of grain refinement and precipitation strengthening. However, when more than 0.4 wt.% Er was added, a coarse Al-Er compound formed on grain boundaries and deteriorated the alloy ductility.

2.4.4 Effect of Sr on Fe-Intermetallics

It was discovered that Sr had a modification effect on Fe-rich intermetallic particles. In a dilute Al-Fe-Si system, iron exists in two major forms-Chinese script α-Al_8Fe_2Si and needle-like β-Al_5FeSi. Some of the reactions occur during the

solidification of a 6xxx aluminum alloy are listed as below (Backerud et al., 1990):

$L+Al_8Fe_2Si \rightarrow Al+ Al_5FeSi$ at ~ 613 °C

$L+Al_8Fe_2Si \rightarrow Al+ Al_5FeSi + Mg_2Si$ at ~ 576 °C

A thin film of silicon was observed around α phase particle in the Sr-doped 6xxx alloy. The Sr absorbed at the surface of α phase and hence acted as a barrier to the silicon diffusion into α phase, and hence inhibited the conversion from α phase into β phase (Samuel *et al.*, 2001).

Strontium (Sr) had also been added to Al-Si cast alloys as a modifier of the detrimental β-Al_5FeSi needles (Suarez et al., 2006). It was found that the addition of Sr refined the eutectic Si as well as secondary β needles, as seen in Figure 2.8 and Figure 2.9. However, the primary β needles became thicker and longer in the Sr doped alloy, whose morphology was more detrimental to the alloy formability than the primary ones in unmodified Al-12Si alloy.

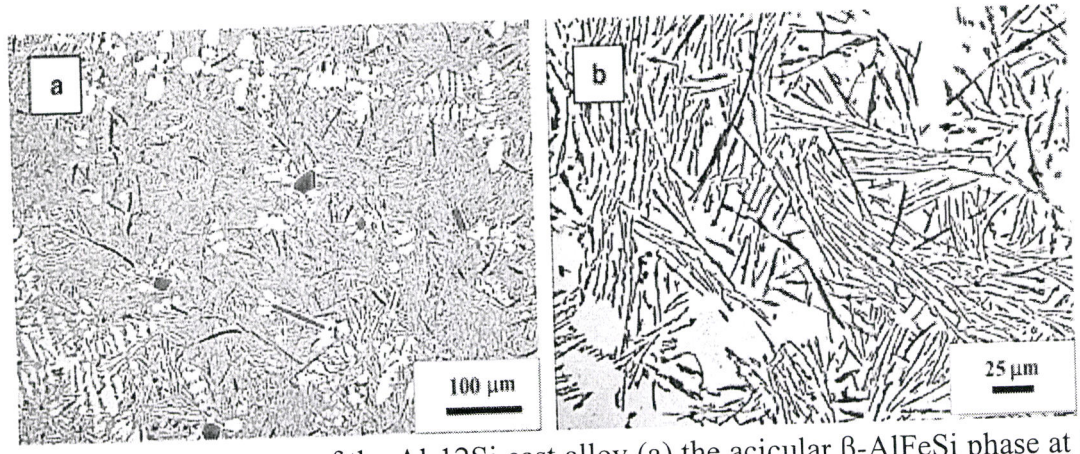

Figure 2.8 Microstructure of the Al-12Si cast alloy (a) the acicular β-AlFeSi phase at low magnification (b) isolated β in matrix at high magnification (Suarez *et al.*, 2006).

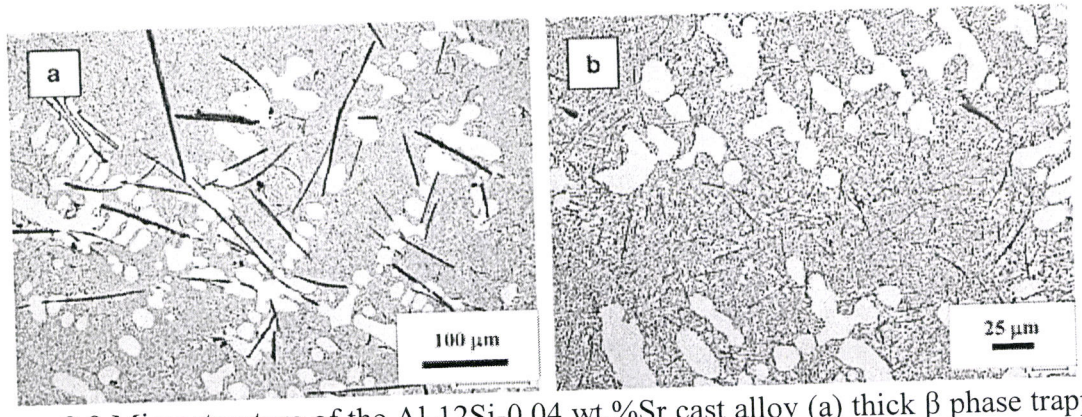

Figure 2.9 Microstructure of the Al-12Si-0.04 wt.%Sr cast alloy (a) thick β phase trapped between Al dendrite (b) thin needles in eutectic silicon phase (Suarez *et al.*, 2006).

Since there was no record to show the Sr modification effect on alloy mechanical behavior, it was uncertain whether such morphology improvement or transformation was sufficient to generate advanced alloy formability. Up to now, the concern of the Sr modification effect was only focused on the β phase. In AA5754 alloy, the silicon content is much lower in comparison with 6xxx alloys. The Al-Fe-Si intermetallics barely exist. Most of the iron will form platelet-like Al-Fe intermetallics, e.g. Al_6Fe, Al_mFe (m=4-4.4) and so on. It would be interesting to see any morphology modification effect happen to

these binary Fe-intermetallic phases. It is also worth examining any formability improvement would be achieved if a chemical modifier, like Sr, was added in AA5754 alloy, .

2.5 Hypothesis of Cerium Modification Theory

2.5.1 Grain Microstructure Refinement Mechanism

Since the cerium has nearly zero solubility in the α matrix, most of its addition would be rejected into the remaining liquid during solidification and form fine $Al_{11}Ce_3$ or Al_3Ce intermetallic compounds between the dendrite arms. In fact, these particles precipitate early in the solidification. They act as heterogeneous nucleation cites and provide grain refinement to the alloy. They also inhibit the movement of dislocations and grain boundaries. The grain size is therefore reduced. As a result of such refinement, the strength and ductility of the as-cast alloy is improved (Ravi *et al.*, 2002).

2.5.2 Intermetallic Refinement Mechanism

Due to the limited understanding of the crystal structures and chemical compositions of the Ce-containing phases in a Al-Mg-Fe system, the underlying mechanism of phase formation during solidification has not been fully understood. It was unknown whether the additions of cerium decomposed the Fe-rich deleterious phase by

diffusing into the particles and hence formed more globular phases, or it absorbed onto the surface of the growing acicular Fe-rich particles, reduced the interfacial energy and shielded it from the melt. No information was available for how the cerium can decomposes the Fe-rich phase or how it would retard the anisotropic growth of the particle.

Since no work has been done on the modification of the acicular Al_3Fe, Al_6Fe intermetallics by small addition of cerium, it would be interesting to see whether the cerium have effect on them, and what mechanisms would be for the modification process.

2.5.3 Secondary Cerium-Containing Phase Strengthening Effect

It was suggested that a secondary cerium-containing phase may precipitate from the supersaturated solid solution during post-casting heat treatment, and hence strengthen the alloys (Xu *et al.*, 2006). Cerium may form secondary Al-Ce particles like the secondary Al_3Er in Al-Mg alloy, or cerium silicide as alleged previously by Barth (1912). Addition of RE element delays the decomposition of supersaturated Al-Mg solid solution (Rokhlin, *et al.*, 2004). This suggests that not many β-Al_3Mg_2 would precipitate from the solid Al. If any of theses phases formed in Al-Mg-Fe alloy, significant increase in its strength would be observed via an artificial aging, and the alloy would transfer from

non-heat-treatable to heat-treatable (Mohamed K. *et al.* 2005).

2.6 Literature Assessment

The addition of cerium has a strengthening effect on various aluminum alloys by providing grain refinement. It is generally accepted that an increase of the volume fraction of particles deteriorates the alloy ductility while the small grain size is in favor of that. Some authors claimed that the alloy ductility was enhanced and the alloy would become heat-treatable after cerium was added (Barth 1912), while others doubted on that. It was observed in high Fe alloy that the addition of cerium affected the morphology of the particles, converting the acicular $Al_{13}Fe_4$ into a more rounded ternary compound (Mondolfo, 1976) enhancing the alloy ductility. This morphology transformation mechanism is still uncertain. It is unknown whether the addition of cerium would form precipitate that behaves like Mg_2Si or secondary Al_3Er, and leads to a heat-treatable Ce-doped Al alloy.

3 EXPERIMENTAL PROCEDURE AND RESULTS

3.1 Al-Mg-Fe Alloy Fabrication

3.1.1 Alloy Design

Fe concentration in commercial AA5754 is generally around 0.2 wt%. Higher iron content would deteriorate the formability of the aluminum alloy. In order to reveal the effect of cerium addition on the acicular iron-rich particles in AA5754 alloys, a reference alloy with iron content up to 0.4 wt% was designed. In order to focus on Fe-rich particles and make the alloy system as simple as a Al-Mg-Fe-Ce system, all the other minor elements such as Mn, Cr, Si and so on were eliminated from the alloy content table. The compositions of the alloys are illustrated as in Table 3.1.

Table 3.1 The designed chemical compositions of the three Al-Mg-Fe alloys

Alloy	Ce	Fe	Mg	Al
Reference	0	0.4	3.5	Rest
0.1Ce	0.1	0.4	3.5	Rest
0.3Ce	0.3	0.4	3.5	Rest

Silicon impurity would deteriorate the formability of the alloy. Cerium silicide or AlFeSi phases, which would interfere with the modification ability of cerium on Al-Fe

phases, would form inside. Although Si has been eliminated on purpose, a little Si could still be introduced as impurity during the alloy fabrication.

3.1.2 Direct Chill Casting and Degassing

Al-Mg-Fe alloys of three compositions were fabricated by a lab simulated DC casting. The aluminum (99.9%) was preheated in the crucible furnace (as seen in Figure 3.1) at 650° C overnight, and melted within two hours after heating to 750 °C. All the surfaces of the crucible were painted with protection layers of boron nitride (BN) to prevent the dissolution of graphite into the melt.

Figure 3.1 The crucible furnace

Fe, Mg and Ce were added in order into the melt. Their purity and adding

temperature are as listed in Table 3.2. Before each addition, the surface layer of aluminum oxide should be removed. After an alloy element was added, the melt was steadily stirred for half an hour and kept for another half hour to let the metal dissolve completely and distribute homogeneously in the molten metal.

Al-Mg master alloy melt immediately. However, this dissolution was accompanied by some sparks of the burning of magnesium. In order to make up this loss of magnesium, extra Al-Mg had to be added if a lower Mg content shown by the chemical composition analysis. Cerium was added twice for the fabrication of 0.1Ce and 0.3Ce alloys. Cerium was very easy to be oxidized. The weighed pure cerium (99.8%) was wrapped in aluminum foils and kept in a vacuumed container. Once taken out, it was added into the melt immediately.

Table 3.2 Materials of AA5754 alloy fabrication

Alloying Element	Fe	Al-Mg master alloy	Ce
Adding Temperature (° C)	800	750	750
Purity(in mass)	99.98%	41%Mg	99.8

Degassing was applied to removing porosity in the cast alloys. The moisture of the metal surface can induce hydrogen porosity in the melt. A rotary degasser, as seen in

Figure 3.2, can remove this porosity as well as the impurity oxidations to the melt surface. Argon gas was injected into the melt through the tube inside the stirrer to remove all these impurities onto melt surface, which can be removed later. The graphite stirrer was also protected by layers of BN. At a 30rpm speed of rotation, the melt was stirred for half an hour. The degassing process made the melt more homogeneous and impurity-free.

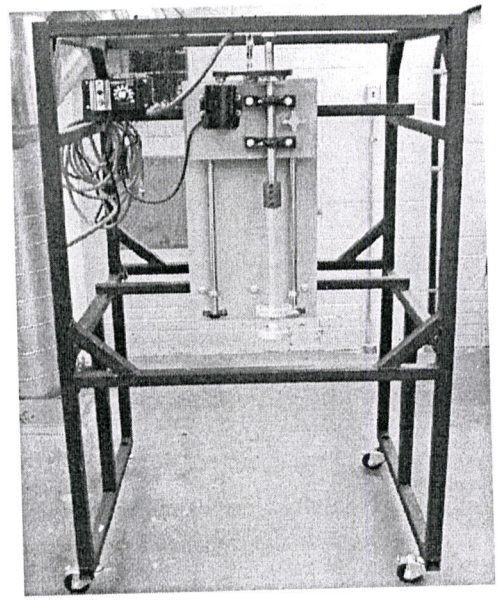

Figure 3.2 Rotary Degasser

Small samples were cast from the melt for alloy composition examination. Adjustment of alloy composition was done according to the result of chemical analysis by GDOES (Glow Discharge Optical Emission Spectroscopy). By adding required amount of metals, a new fabricated alloy sample was sent for chemical analysis again.

Degassing was repeated once new metals were added. When the expected chemical composition was achieved, an amount of the melt was poured into a water-quenched copper mould, to cast ingots with a size of 2" by 2" by 10". These were marked as reference alloy, 0.1Ce and 0.3Ce respectively.

Later, the chemical compositions of the three alloys were reexamined by ICP (inductively coupled plasma), which had more accuracy for detection of minor elements, like the Ce. The investigated chemical composition were illustrated as in Table 3.3. All of the three compositions of cast alloys have a magnesium level around 4 wt.%, and a Fe level around 0.4 wt.%. The AA5754 alloys with respective cerium level of 0.13 wt.% and 0.31wt.% were achieved successfully. No silicon and other metallic elements were detected.

Table 3.3 Chemical compositions of as-cast alloys

Alloy	Ce	Fe	Mg	Al
Reference	0	0.39±0.01	3.9±0.1	Rest
0.1Ce	0.13±0.02	0.40±0.01	4.2±0.1	Rest
0.3Ce	0.31±0.01	0.39±0.02	4.0±0.1	Rest

3.2 Thermomechanical Processing Schedule

Since the mechanical property test specimens should be taken from the Al-Mg-Fe sheet alloys, all the cast alloy ingots have to go through a series of processing to be made into alloy sheets. Thus we mostly followed an industrial thermo-mechanical schedule for AA5754 alloy, as shown in Figure 3.3.

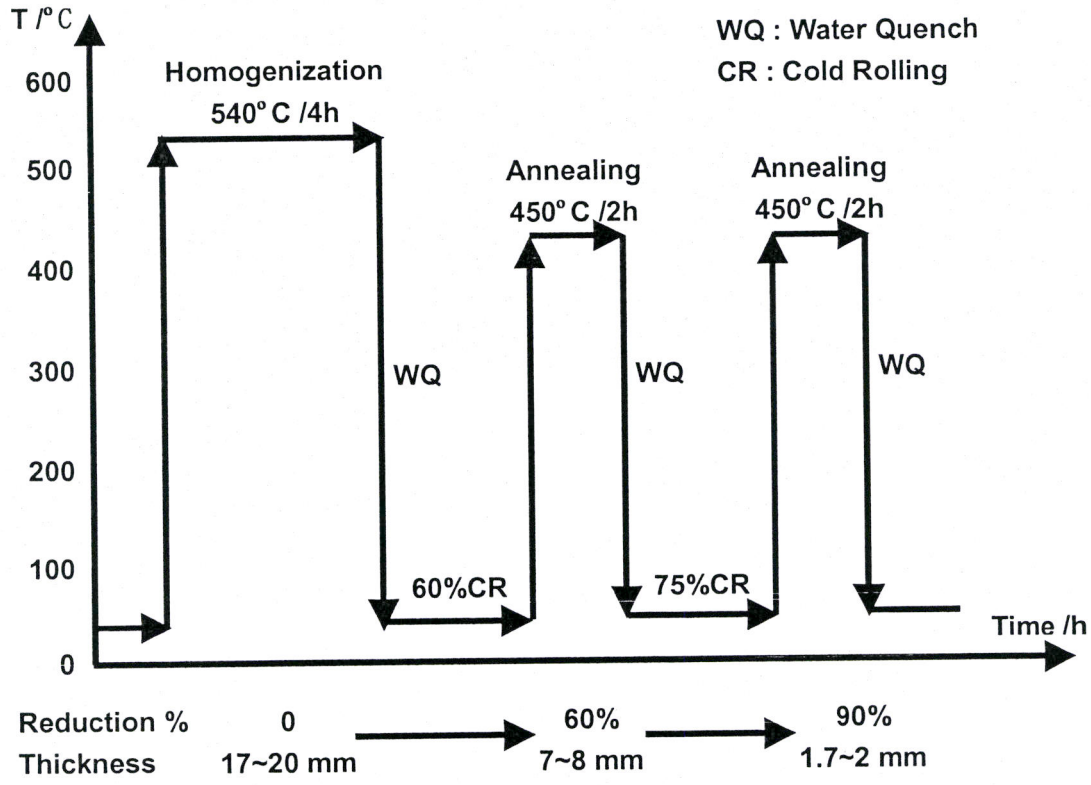

Figure 3.3 Thermo-Mechanical Processing Schedules of AA5754 Alloys (Girard, 2002)

3.2.1 Homogenization

The coring of magnesium in the cast Al-Mg alloys can be removed by a homogenizing anneal. During this process, the as-cast alloys are heated at a temperature slightly below the solidus for a sufficient time to allow alloying elements to diffuse to less-concentrated regions, in order to attain a homogeneous distribution of solutes.

By Fick's Laws, the time for heat treatment can be roughly estimated as below,

$$D = D_0 \exp(-\frac{Q}{RT}) \text{ and } \lambda = \sqrt{Dt}$$

$$t = \frac{\lambda^2}{D} = \frac{\lambda^2}{D_0 \exp(-\frac{Q}{RT})}$$

where D is the real diffusion coefficient, D_0 is the pre-exponential term of the diffusion coefficient of the element, t is the time for diffusion, T is the temperature of heating, Q is the activation energy for diffusion, and R is the gas constant.

In the cast Al-Mg alloys, the required distance for diffusion of magnesium could be estimated as the dendrite spacing. Here, if we supposed that $\lambda \approx 50\mu m = 5\times10^{-5} m$, with $D_{o,\ Mg\ in\ Al} = 2.3\times10^{-4} m^2/s$, $Q = 131 kJ/mol$, $T = 500°C$ (Brandes *et al.*, 1992), the time was estimated approximately as 2 hours. Similar calculation was done to Fe and Ce (Cai, 2002), which turned out to be above 24 hours. Since it was unpractical to

give such long time of high temperature heating to the alloys, and since it may result in thermo-corrosion and coarse grain structure due to overheating, the homogenization was given only for the time required for magnesium diffusion.

As an empirical routine, the time should be given as double of the estimated one, so as to promise the completeness of diffusion. Therefore, the alloys were kept in an air furnace at 540 °C for 4 hours, followed by water quenching in order to prevent any precipitation. This will be explained in the following aging section.

3.2.2 Cold Rolling and Intermediate Annealing

Homogenized alloys were cold rolled to 60% reduction in thickness. Once the material is highly deformed, it is strong and brittle. In order to make the following cold deformation of the alloys easier and more homogeneous, intermediate annealing was given to the rolled AA5754 alloys. After heating at 450° C for 2 hours in the air furnace, recrystallisation was completed, and the sheet alloys become soft again. It could be easily rolled for another 75% reduction in thickness, down to the final thickness of ~2mm.

3.2.3 Annealing

As our aim of the following tests is to examine the formability of the materials, the sheet alloys are all annealed again at 450° C for 2 hours to release the stress and complete the grain recrystallisation, so as to attain good ductility.

AA5754 alloy is non-heat-treatable. After addition of cerium, it was unknown whether any precipitation hardening would happen to this alloy and change it into a heat-treatable one. Aging and hardness tests can be done to the modified AA5754 alloys. Therefore, all the samples should be prepared as water quenched after any heat treatment.

3.3 Metallographic Examination

3.3.1 Grinding and Polishing

Samples were cold mounted in Araldite for metallographic examination. An automatic polisher with programming was used for grinding and polishing.

Grinding started from 1200 SiC paper and lasted for 4 minutes with running water as lubricant and finished with 4000 grit paper for 3 minutes. Then, the samples were polished with 3 μm and 1μm diamond solution for 6 minutes and 4 minutes respectively.

The 0.05μm colloidal silica was used for the final polishing step. Between each grinding and polishing step, the sample surfaces were washed with synthetic cotton and pH neutral liquid soap, rinsed with ethanol and air dired. Once polishing was completed, all samples should be immersed in ethanol and put in ultrasonic bath for 1 minute to remove the residues on sample surfaces.

3.3.2 Electrolytic Etching

Barker's reagent is used to anodize the as-polished sample surfaces. The 2.5% HBF_4 etchant was poured into the automatic electrolytic etcher Polectrol as shown in Figure 3.4. The power supply was set at DC 27 V and the polishing lasted for 1 minute. Once finished, the sample was rinsed under flowing hot water for one minute and then forced air was used to blow them dry. The grains would appear in different colors with optical microscopy under polarized light.

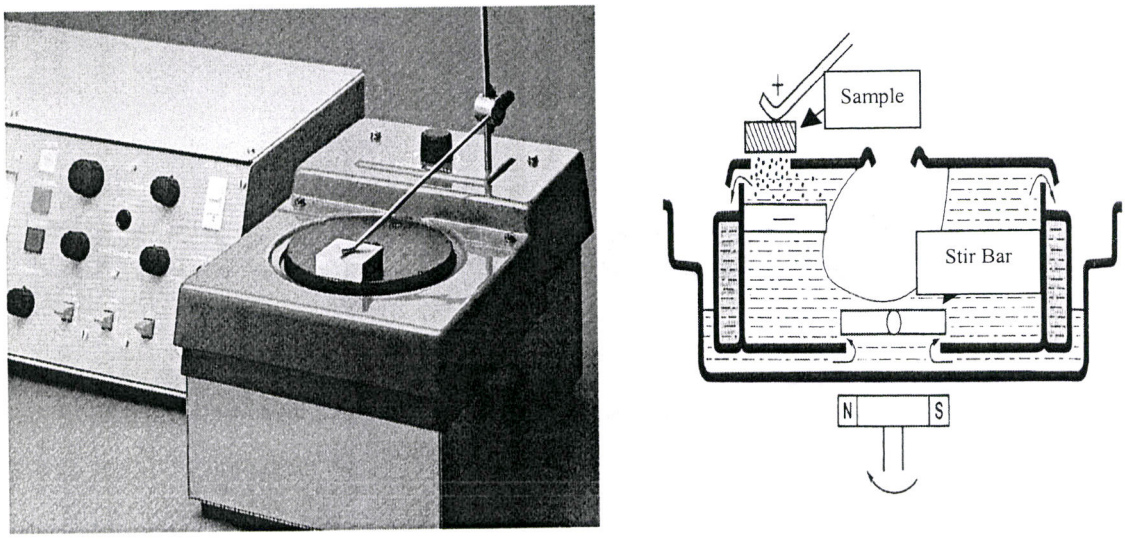

Figure 3.4 Polectrol electrolytic polishing and etching apparatus

3.3.3 Grain Size Measurement

The grain size of a sample can be estimated based on observations of the grain structures. With the aid of a quarter wavelength plate, pictures of an anodized sample surface were taken under cross-polarized light with the Axioplan 2 Imaging and Axiophot 2 Universal Microscope. Arbitrary lines can be drawn across these colorful grains by image analysis software Northern Eclipse Version 6.0. After calibration of the measuring tool, the intercept length of the lines between successive grain boundaries can be calculated for the grain size estimation. As the polarizer rotated, the colors of grains changed gradually and a few grain boundaries disappeared while others showed up.

Therefore, the measured grain size was actually larger than real value.

Grain sizes of the as-cast and thermo-mechanically processed alloys were measured at the L-ST plane (section plane parallel to rolling direction). 10 pictures were taken across the surface of the specimen, and 5 times measurement of grain size was done on each image. Statistical data were collected and the result was given in Table 3.4.

Table 3.4 Grain Sizes of AA5754 Alloys (in microns)

	Reference	0.1 wt. % Ce	0.3 wt. % Ce
As-Cast	146±4	97±5	104±4
60% Reduction Cold Rolled and Annealed	17.1±0.4	15.4±0.2	16.8±0.1
90% Reduction Cold Rolled and Annealed	15.6±0.2	14.8±0.05	15.3±0.1

As shown in Table 3.4, for the group of as-cast alloy, the grain size of AA5754 alloy was reduced by at least 40 microns in the 0.1Ce alloy. However, no further decrease of grain size was measured in the 0.3Ce alloy. For example, images of anodized grain structures of reference, 0.1Ce and 0.3Ce samples were presented in Figure 3.5-Figure 3.7 respectively. It was clear that, the grain structure of as-cast AA5754 alloy was coarse in the as-cast alloy but fine and similar in the 0.1Ce alloy and 0.3Ce alloy. Therefore, the addition of cerium had a limited refinement of grain structure on the as-cast AA5754 alloy.

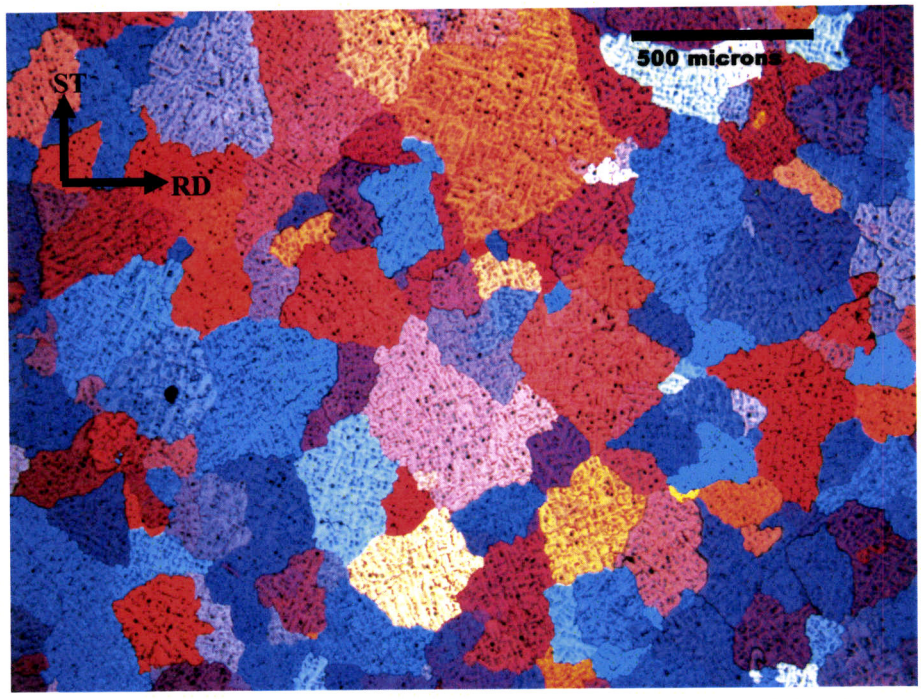

Figure 3.5 Grain structure of as-cast reference alloy

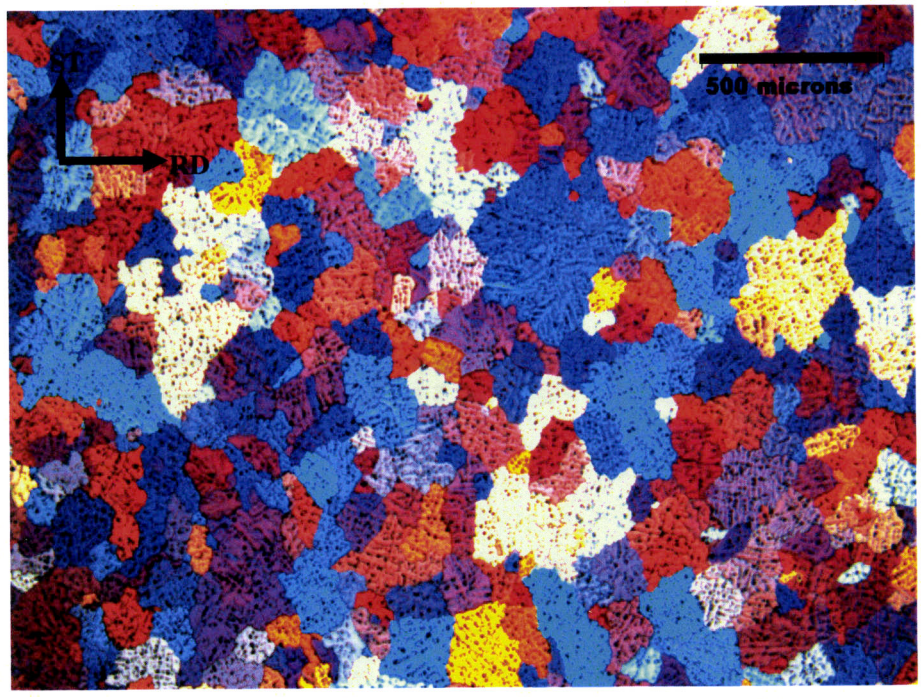

Figure 3.6 Grain structures of as-cast 0.1Ce alloy

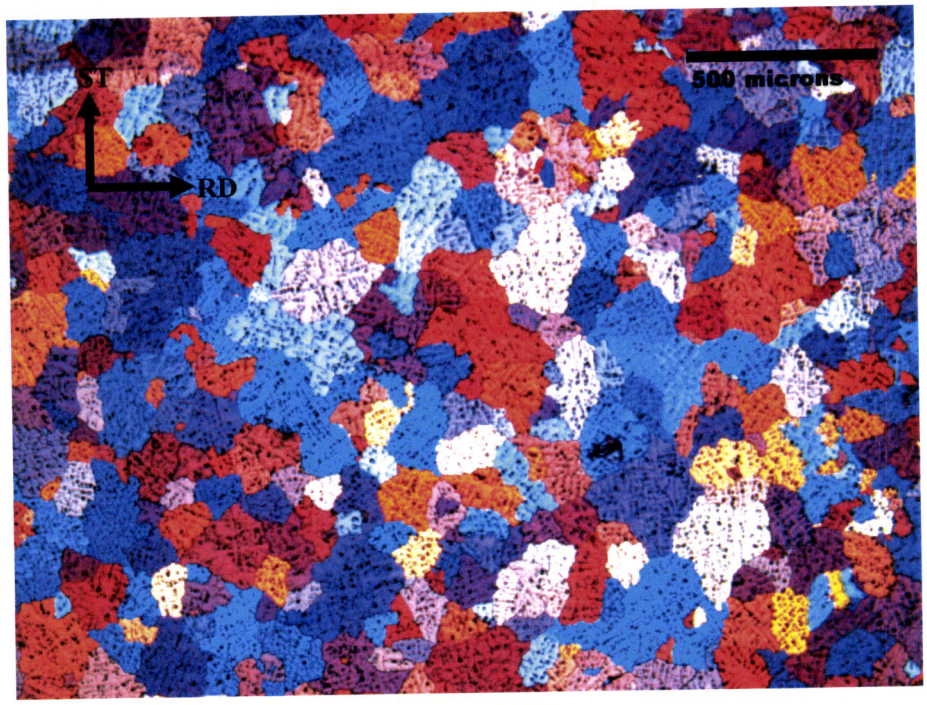

Figure 3.7 Grain structures of as-cast 0.3Ce AA5754 alloy

The grain structures of three composition alloys were all refined after 60% reduction cold rolling and full annealing. Although the 0.1Ce alloy still attained the smallest grain size, the difference of three alloy grain sizes was within 2 microns. Images of anodized grain structures of the group of the 60% reduction cold rolled and annealed alloys were presented in Figure 3.8Figure 3.10. It is noticed that the dendrite structures disappeared in the grains, and most of the particles formed in stringers along the rolling direction.

Therefore, during the thermo-mechanical processing, the grain structures of all alloys were refined. The difference of grain sizes in three composition alloys was almost

diminished. All the grain structures were refined to a similar degree that the grain sizes were the same. The advantage of cerium-doped alloy on grain structure was eliminated by the thermo-mechanical processing.

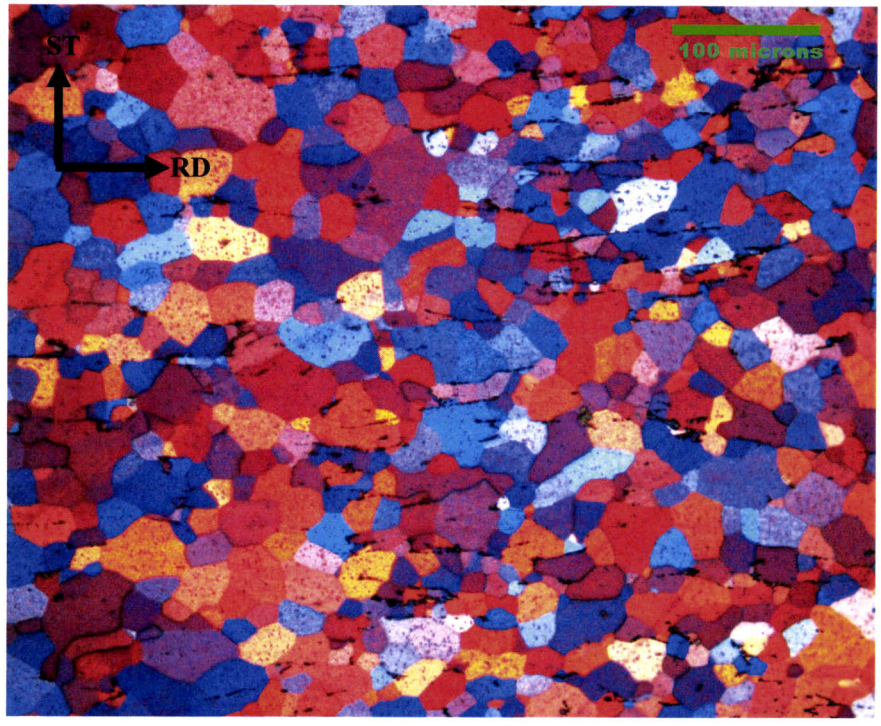

Figure 3.8 Grain structure of 60% reduction cold rolled and annealed reference alloy

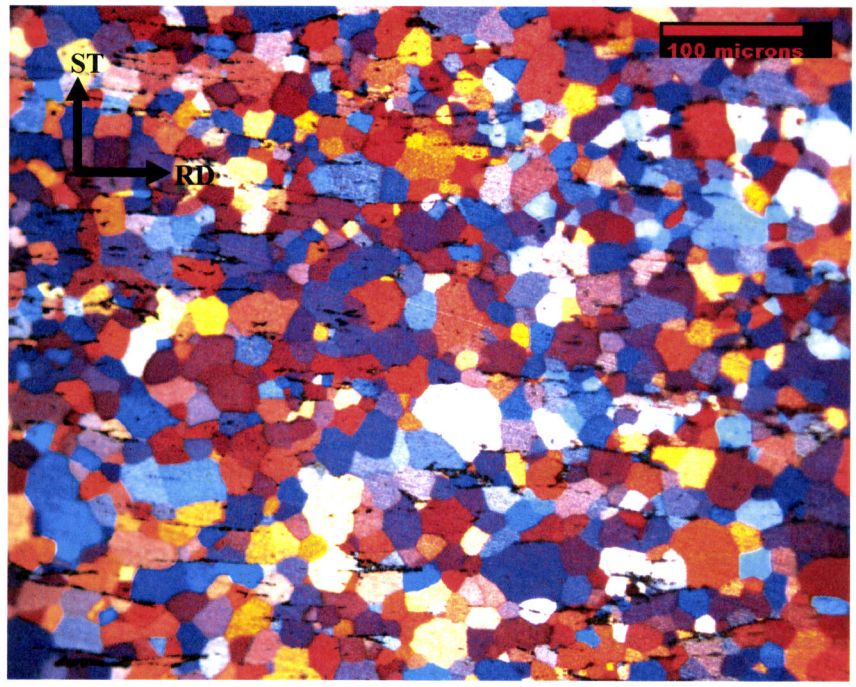

Figure 3.9 Grain structure of 60% reduction cold rolled and annealed 0.1Ce alloy

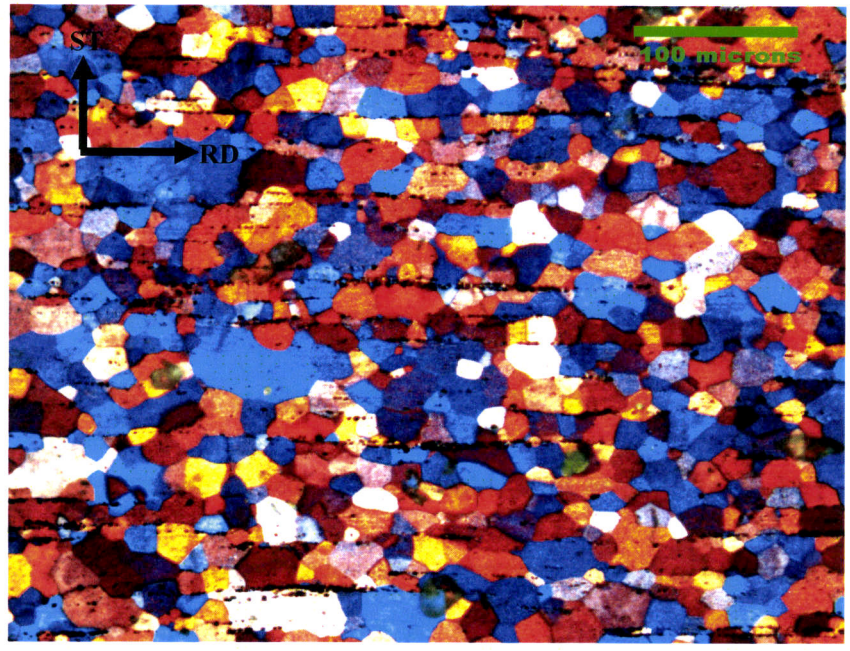

Figure 3.10 Grain structure of 60% reduction cold rolled and annealed 0.3Ce alloy

Measurements in Table 3.4 indicated that, compared with the 60% reduction group alloys, the grain size after 90% reduction only decreased about 2 microns. The grain size differences among the reference alloy and 0.1Ce and 0.3Ce alloys was further decreased and were negligible.

Therefore, the grain structure of AA5754 was refined both by the addition of cerium and the thermo-mechanical processing. The difference in grain size of three composition alloys was almost diminished after 90% reduction cold-rolling and fully annealing.

3.4 Metallographic Observation

3.4.1 Intermetallic Morphology in As-Cast Alloys

The dominant phases in the reference alloy should be Fe-rich phases, which appear either as needle-shape stable $Al_{13}Fe_4$ or rod-like metastable Al_6Fe. Due to the fast cooling rate of the water quenched copper mould, a lot of metastable Al_6Fe and Al_mFe (m=4~4.4) and Al_xFe (x=5~5.8) phases form in the cast alloys (Kosuge *et al.*, 1972).

As seen in Figure 3.11, an elongated intermetallic compound with lengths of

several microns was observed in the picture A and marked as phase 1. The EDS analysis result indicated this intermetallic compound was an iron-rich particle. More similar needle-like particles were observed at a lower magnification of ×350 in B. Again, the EDS analysis results confirmed that they all belonged to the phase 1. Therefore, it could be concluded that the Fe-rich particles, which was labeled as phase 1 in A and B, dominated the second-phase coarse constituents in the reference AA5754 alloy.

In the 0.1Ce alloy, three different phase morphologies were observed in the C and D. Elongated particle were marked as phase 1, small spheroids were marked as phase 2, and short rod-like particles were marked as phase 3. EDS analysis results showed that, the phase 1 particle was same as the Fe-rich particle in reference alloy. The phase 2 particle is a cerium-rich intermetallic compound, and the phase 3 particle is an Al-Fe-Ce second-phase constituent.

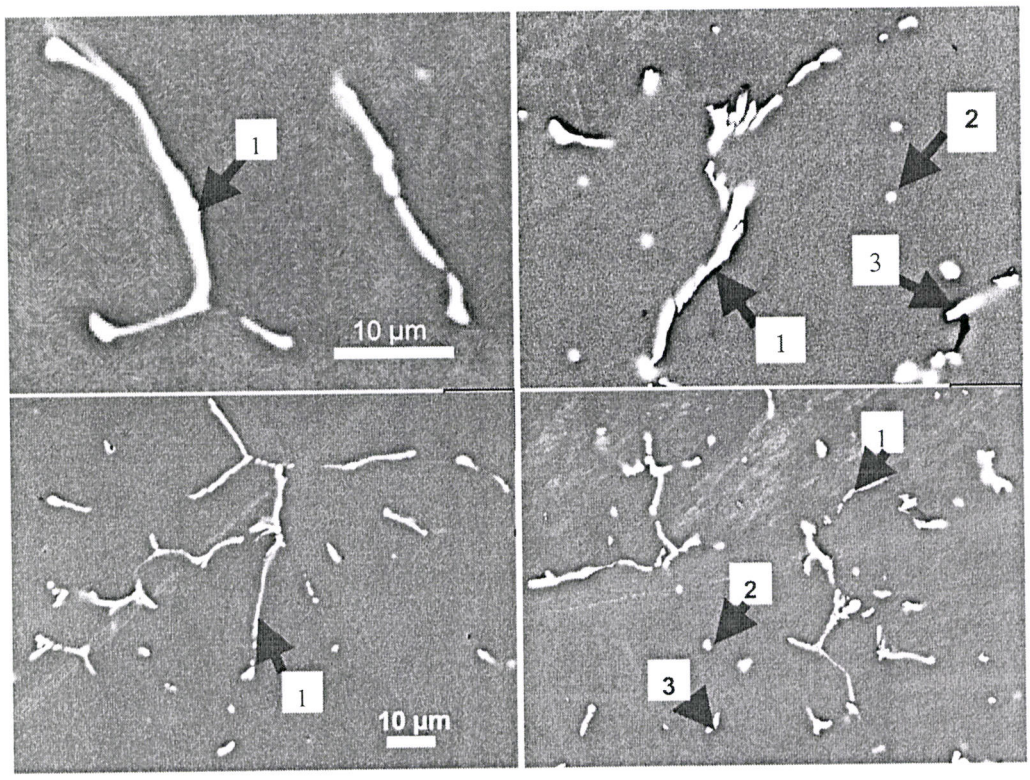

Figure 3.11 SEM metallographic observation of the Intermetallics in as-cast reference alloy (A at x1000 and B at x350) and as-cast 0.1Ce alloy (C at x1000 and D at x350), at BSE Mode. Phases of the intermetallics in Al matrix are 1: Fe-rich binary phase; 2: Ce-rich binary phase ; 3 :Al-Fe-Ce ternary phase.

As seen in pictures B and D, the appearance of these tiny spheroids and short rods increased the total volume fraction of intermetallics. The elongated Fe-rich intermetallics still dominated the intermetallics in the 0.1Ce alloy, however, it seemed that these needles became thicker and shorter after the addition of cerium.

3.4.2 Intermetallic Morphology in Rolled Alloys

Twenty SEM pictures of the microstructures at the L-ST (longitudinal transverse section plane) were taken for each of the reference and cerium-added alloy. As seen in Figure 3.12, after 60% reduction cold rolling, all the big particles broke into small ones of a few microns and formed stringers along the rolling direction. The interspacing of particles in these stringers was much smaller than those of isolated ones. The length and size of these stringers varied a lot within one sample. Generally, no measurable difference of intermetallic morphology was observed in the reference and 0.1Ce alloy. However, the volume fraction of the intermetallics would have influence on the alloy properties.

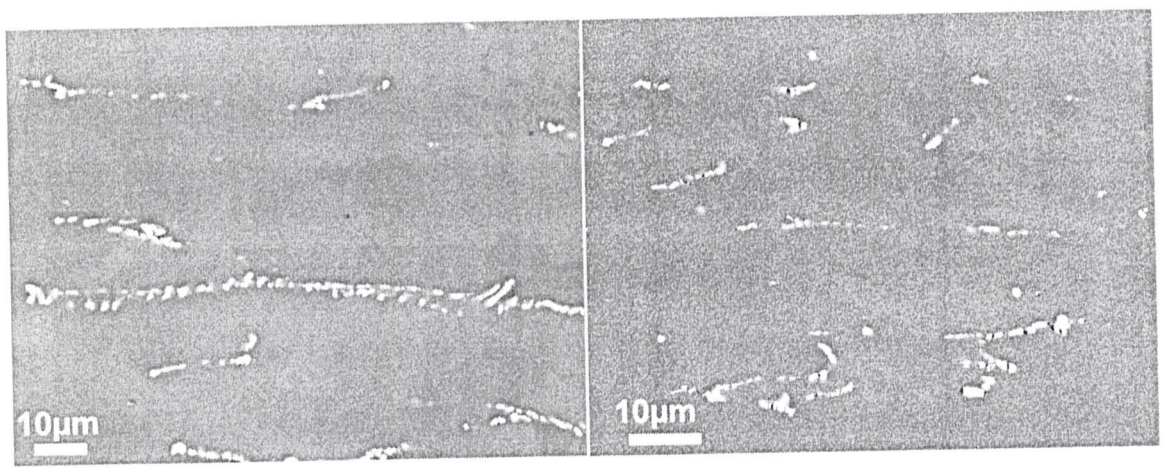

Figure 3.12 Stringers formation in 60% cold-rolled reference alloy (left) and in 0.1Ce alloy (Right) at L-ST plane.

3.4.3 Volume Fraction and Shape Factor

The shape factor was defined by the formula $(4\pi \cdot \text{Area})/(\text{Perimeter})^2$ (as seen the Northern Eclipse Manual in the Appendix), which is in an inverse relation to the aspect ratio. A perfect round particle would have a shape factor close to 1, while a thread-like object would have a shape factor about zero. Besides their sizes, the shape factors of intermetallic compounds also had significant influence on the mechanical performance of the alloys. Hence, the percentage of intermetallics with large shape factor was also measured for each alloy. Because the shape factor of a small rod-shape particle was around 0.55, in order to count the spheroids and short rods in the alloy, the measurement was only counting on particles with shape factor larger than 0.55.

A combination of low volume fraction and large shape factor of intermetallics would be in favor of better formability. SEM pictures of the microstructures were taken on the casting direction plane for all the as-cast alloys and on the L-ST plane for the 60% reduction and annealed alloys. With the aid of image analysis software Eclipse 6.0, the volume fractions of these particles and their shape factors were quantified.

As seen in Table 3.5, a slight increase was observed in the volume fractions of particles after the addition of cerium in the alloys. Measurable increase in the percentage

of high shape factor particles was only detected in as-cast 0.3Ce alloy. This increase could be attributed to the extra addition of cerium. In rolled and annealed alloys, the particle volume fraction was decreased while the average percentage of round particles was increased after the thermo-mechanical processing. When an alloy was deformed, its particles broke into small round ones. Since the volume fraction of particles was in fact based on the data of area fraction of particles on the L-ST plane, the results given in Table 3.5 could only be an rough estimation of the particle volume fraction.

Table 3.5 Volume fractions of intermetallics and fractions of intermetallics with shape factors larger than 0.55 (in %)

	Reference	0.1 wt.% Ce	0.3 wt.% Ce
		As-Cast	
Intermetallic Volume Fraction	2.1±0.02	2.24±0.03	2.42±0.02
Average Fraction of Particles with Shape Factor ≥0.55	0.18	0.19	0.24
		60%Cold Rolled & Annealed	
Volume Fraction	1.64±0.02	1.7±0.01	1.89±0.01
Average Fraction of Particles with Shape Factor ≥0.55	0.4	0.5	0.32

Quantification results indicated that the volume fraction of intermetallics increased by the addition of cerium. The average aspect ratio of intermetallics decreased due to the reduced volume fraction of elongated particles.

3.5 Particle Extraction by Phenol Dissolution

Intermetallics embedded in the Al matrix can be extracted by phenol dissolution method . Around a 4 gram sample of each alloy was prepared and dropped into 100ml of slightly boiling Phenol. After the dissolution was completed, a mixture of 80ml of Benzyl alcohol and 20 ml of Toluene was added to the Phenolic solution and centrifuged for 60 minutes. The liquid was then decanted. Another mixture of 50 ml Benzyl and 50 ml Toluene was added, and the centrifuging repeated. This washing and centrifuging cycle was repeated several times. Afterwards, the bottles containing the decanted liquid were moved into an oven to dry the residue. Thus the intermetallics were extracted and ready for XRD analysis and EDS semi-quantification.

The extracted particle powders were weighed and the corresponding intermetallic weight fractions of as-cast alloys were calculated and given in Table 3.6. Generally, the addition of cerium increased the weight fractions of intermetallics. However, as the β -Al_3Mg_2 were dissolved by phenolic solution and part of the fine particles might be lost during the decantation, the real weight fraction of intermetallics should be larger than the weighed ones. In order to know how cerium increased the weight fraction of the intermetallics, phase identification was done on these powders.

Table 3.6 Weight fraction of intermetallics in as-cast AA5754 alloys

	Reference	0.1wt % Ce	0.3 wt % Ce
Weight Fraction of Intermetallics (in wt %)	1.14	2.13	1.98

3.6 Phase Identification

3.6.1 Phase Predication in Al-Mg-Fe Alloy

From the Al-Ce phase diagram (as seen in Figure 3.13), cerium could form the binary phase $Al_{11}Ce_3$ (or Al_4Ce) or Al_3Ce in the Ce-doped Al alloy.

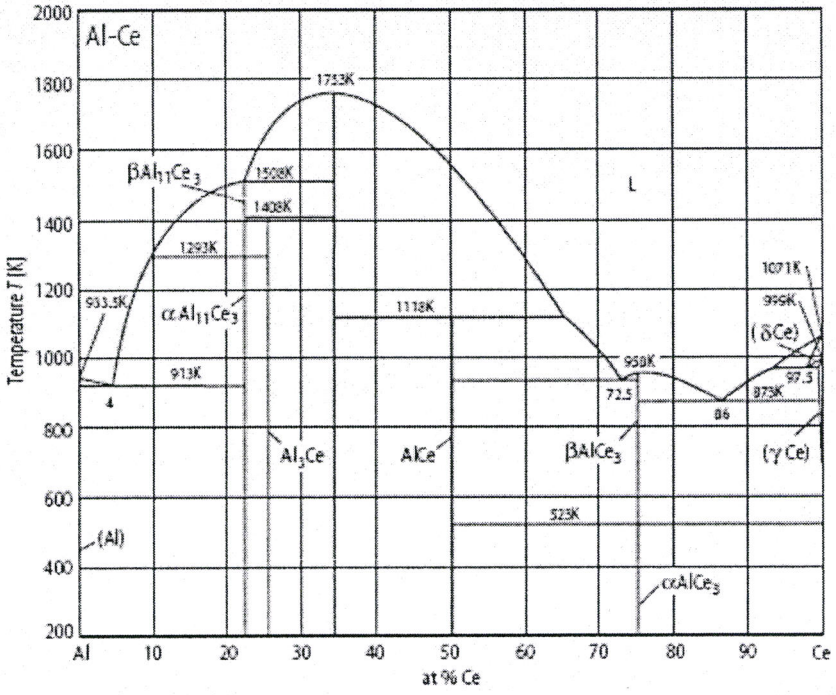

Figure 3.13 The Al-Ce binary Phase Diagram (Landolt-Börnstein Group IV., Vol. 5a, 1991)

For the Al-Fe-Ce system, Thiede *et al.* (1998) reported the only one cerium-containing ternary phases $Al_{10}CeFe_2$ (26.7% Ce, 21.6% Fe). However, the stable $Al_{11}CeFe_3$, Al_8CeFe_2, Al_8CeFe_4, and the metastable $Al_{10}CeFe_2$ and $Al_{20}CeFe_5$ are also possible ternary phase in a Al-Fe-Ce system (seen Landolt-Börnstein in Appendix).

Since the compositions and thermo-mechanical processing history of AA5754 alloys varied a lot, the phases contained were still uncertain. It is hoped that by thermodynamic calculation, the phases formed during the solidification process can be predicted. Therefore, Thermo-calc was applied for the modeling of the solidification process of Al-Mg-Fe and Al-Mg-Fe-Ce system respectively. Scheil-Gulliver formalism was applied to the redistribution of alloy elements between the growing FCC phase and the remaining melt phase.

According to Figure 3.14, the FCC Al matrix was the major solid phase in the Al-4Mg-0.4Fe system. Around 600 °C, it completes its formation. The precipitation of $Al_{13}Fe_4$ started at around 640 °C and ended slightly above 600 °C, even before the Al matrix completed its formation. The β-Al_3Mg_2 started precipitating around 210 °C.

It is clearly shown in Figure 3.15 that in the cerium containing alloy, $Al_{11}Ce_3$

appeared and increased the total weight fraction of intermetallic phases. Similar to $Al_{13}Fe_4$, it also completed formation within a shallow temperature range, slightly below 600 °C.

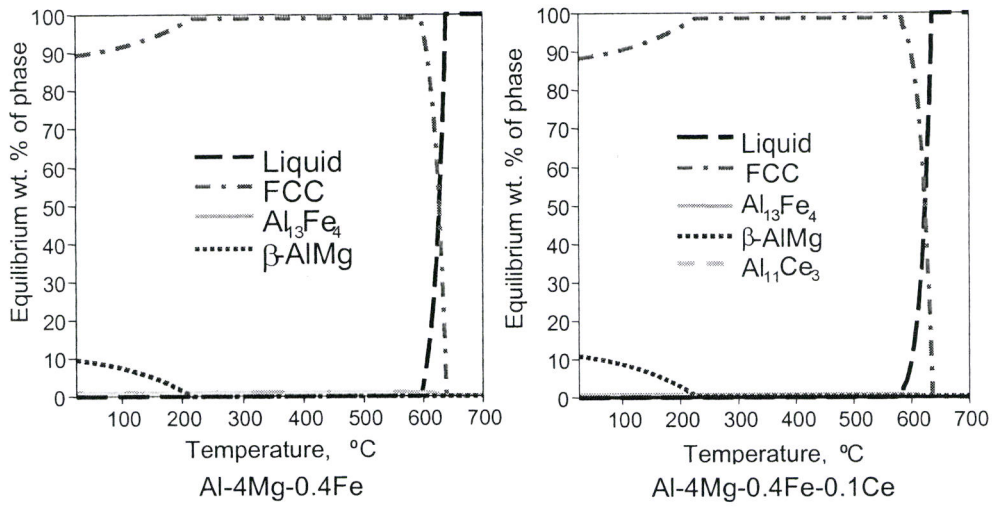

Figure 3.14 Weight fractions of phases formed during solidification

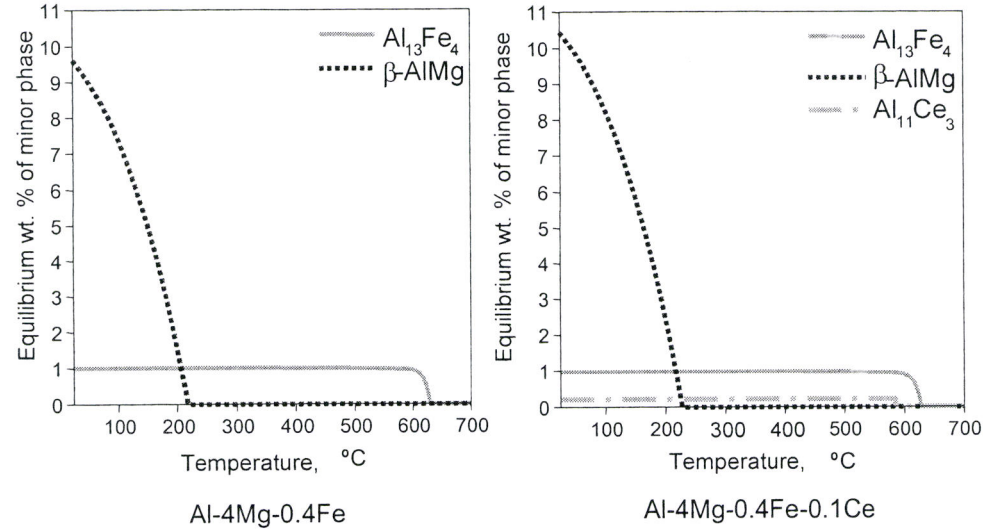

Figure 3.15 Weight Fractions of Intermetallics Formed During Solidification

The data for ternary and quaternary systems was unavailable, this modeling was built upon binary systems. Thus, the predicted phases could be incomplete without considering possible ternary or even quaternary phases. At different cooling rate and thermo-mechanical processing stage, the Fe-rich particles might appear in different forms which even not included in phase diagram. Therefore, a laborious experimental investigation of phase identification is necessary to examine and confirm the predication results.

3.6.2 XRD Analysis

Intermetallic phases can be identified by X-Ray Diffraction (XRD). X-ray diffraction profiles of intermetallic powders of reference alloy, 0.1Ce alloy and 0.3Ce alloy are shown in Figure 3.16-Figure 3.18 respectively. The Al-Fe phase, eg. Al_6Fe and Al_mFe, had the highest intensity peaks in each profile. This meant that they dominated the intermetallics powders.

In the reference alloy, as seen in Figure 3.16, the major second phase constituent particle is Al_mFe. Correlated with previous EDS analysis results on the as-cast alloys, it can be predicted that Al_mFe is the phase with a dendrite morphology in the Al matrix. A very low peak of Mg_2Si and Al_2O_3 indicated their negligible existence in the reference

alloy. Other unidentified peaks probably represented unknown iron aluminide phases.

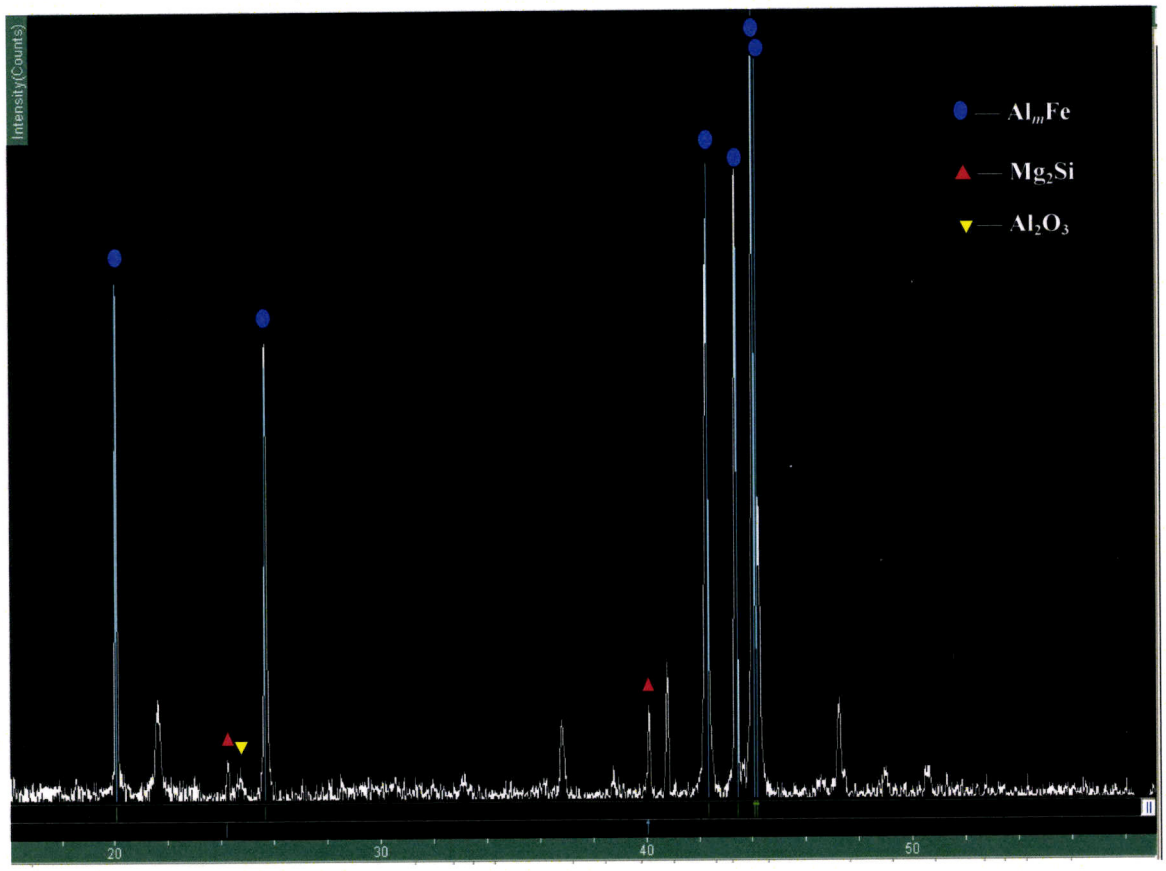

Figure 3.16 XRD spectrum of particles extracted from as-cast reference alloy

In Figure 3.17 and Figure 3.18, Ce-containing binary and ternary phases formed in 0.1Ce and 0.3Ce alloys. According to the peak heights of the phases, the major cerium-containing phase was Al_4Ce (Landolt-Börnstein Group IV. Vol 5a, 1991). Correlated with previous EDS analysis results on the as-cast alloys, it can be predicted that Al_4Ce is the phase with a spheroid morphology in the Al matrix. Ternary phase

Al_8CeFe_2 (Landolt-Börnstein Group IV. Vol. 5a, 1991) was also detected with a very low peak, which indicated its low concentration in the 0.1Ce alloy. In the XRD spectrum, two peaks at 22 and 34 degree, pointed by arrows, were unidentified new phases.

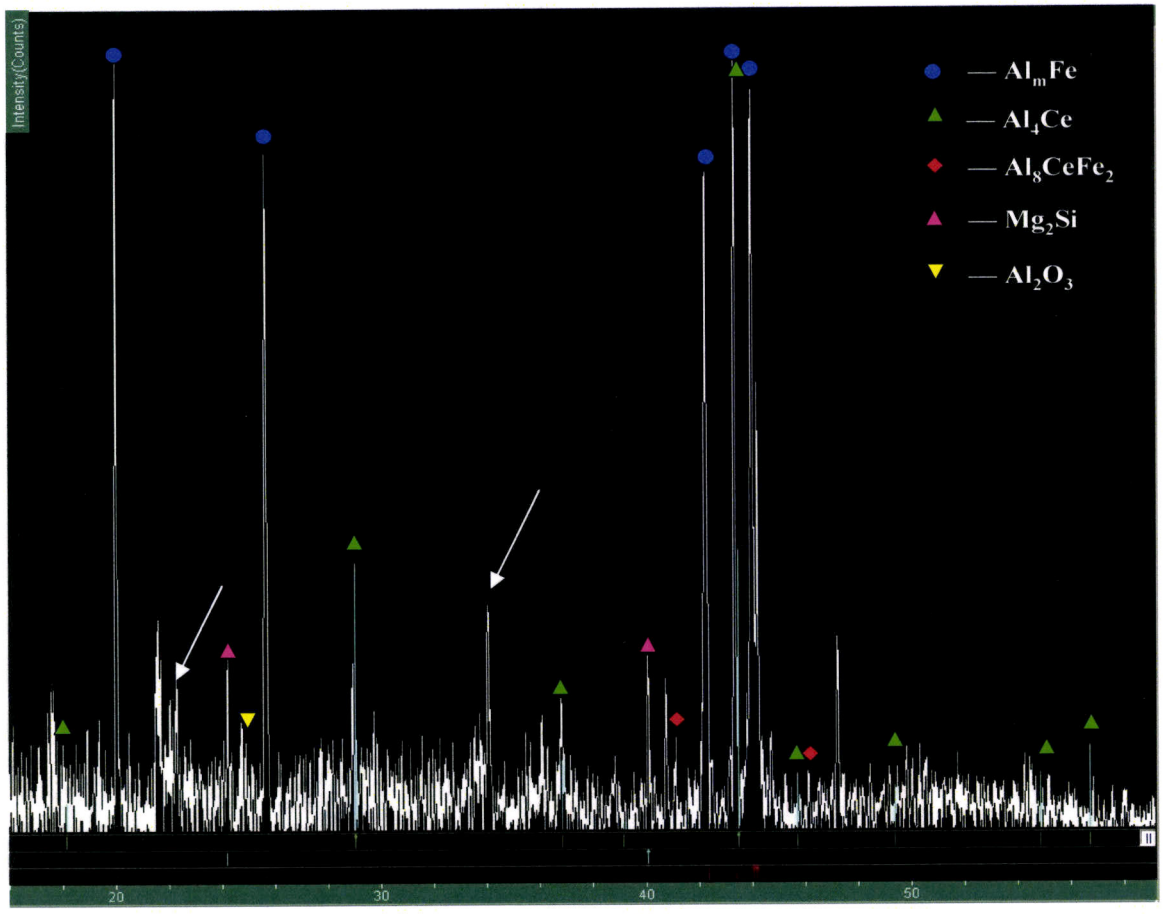

Figure 3.17 XRD spectrum of particles extracted from as-cast 0.1wt.% Ce alloy

As shown in Figure 3.18, more kinds of intermetallic compounds appeared in the 0.3Ce alloy. Extra addition of cerium led to the significant increase of the Al_4Ce phase.

Tiny amount of new binary phase $Al_{92}Ce_8$ also appeared in the profile. The intensities of ternary phase Al_8CeFe_2 was as weak as in 0.1Ce alloy. In addition, the appearance of Al_6Fe indicated that more Fe-rich phase formed. Few Al_3Mg_2 and $Al_{12}Mg_{17}$ peaks appeared in the XRD profile. These might be attributed to not dissolved Al-Mg dispersoids in the 0.3Ce alloy. Similarly, in the XRD spectrum, two peaks at 22 and 34 degree, pointed by arrows, were unidentified new phases.

Therefore, Al_mFe and Al_4Ce were the major second phases in as-cast 0.1Ce alloy , and the Al_mFe, Al_6Fe and Al_4Ce were the major second phases in 0.3Ce alloy. The extra addition of cerium in 0.3Ce alloy did not generate more Ce-containing ternary phases or many new cerium-rich phases. Rather, it seemed to promote the formation of more Al_mFe and Al_6Fe phase in the 0.3Ce alloy. It was known that the additional alloying elements would make the solid solution more saturated and promote their precipitations from the Al matrix.

In Figure 3.17 and Figure 3.18, there were a few peaks around 22 and 34 degree which were unidentified. Besides Al_6Fe, the addition of cerium in 0.3Ce alloy also promoted the formation of the unknown phases. These unidentified phases were not reported in literature, which could be Fe-rich, or Ce-rich or both Fe and Ce containing.

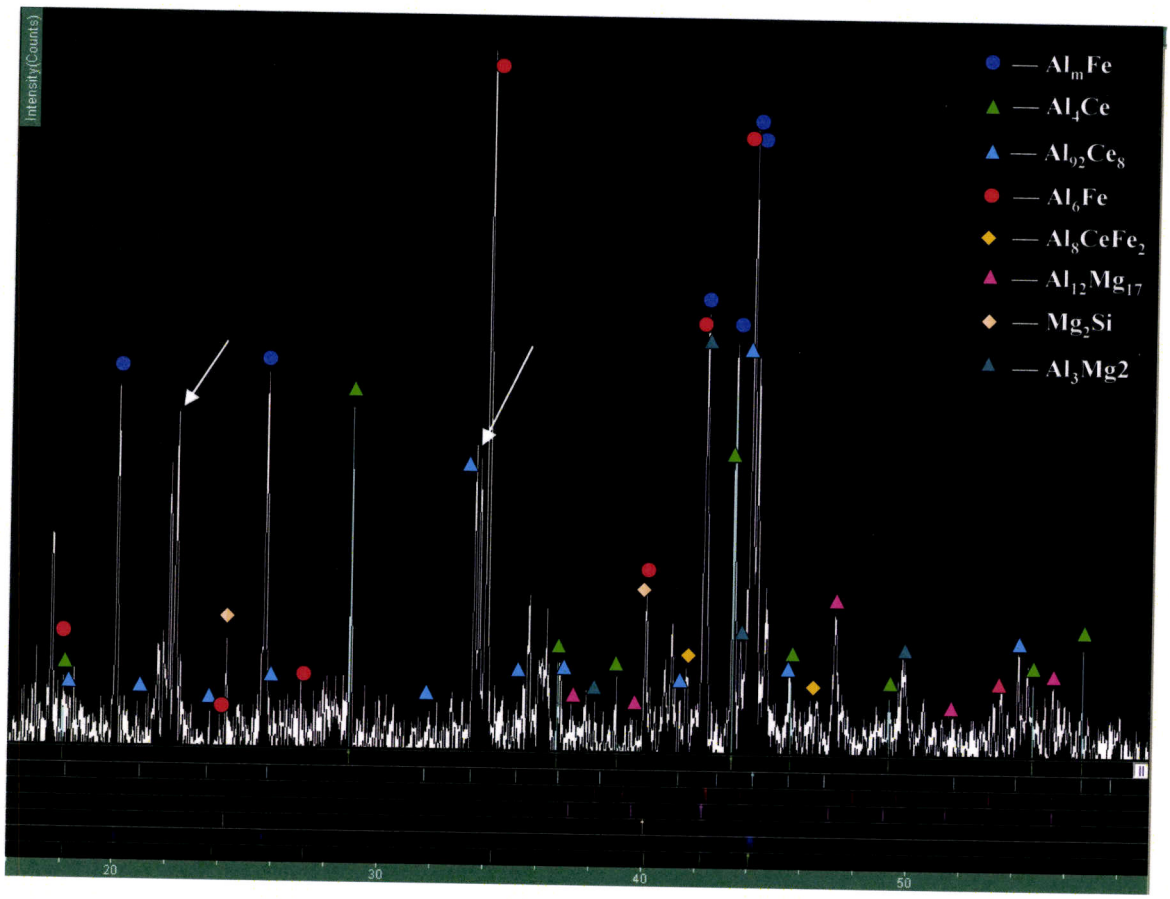

Figure 3.18 XRD spectrum of particles extracted from as-cast 0.3 wt.% Ce alloy

3.6.3 EDS Analysis

A small amount of the intermetallic powder was mixed with 35 ml ethanol and sonicated to resolve the intermetallic powders. A drop of this solution was then placed onto a disk of graphite. The particles were sent to SEM/EDS observation. Since the background is graphite, the elemental signals from particles would no longer be

interfered with those from Al matrix. With an acceleration voltage 10 keV, working distance of 10 microns, images were taken in secondary electron mode and EDS were done with a background signal of carbon. The composition of the phases could be estimated by the semi-quantification of EDS.

In the as-cast alloy, most of the Fe-rich intermetallic particles formed as dendrites with needle-like or platelet-like tips (Liang and Jones, 1993). In Figure 3.19, the coarse constituent particles had sizes of several microns. Their morphologies appeared as Chinese script or irregular elongated needles and rods. EDS analysis result, as seen in Table 3.7, indicted that all these intermetallics were the Fe-rich phase. Also few of them contained cerium. According to a rough estimation of their compositions, these particles could be attributed to the binary phases of Al_6Fe, Al_mFe (m=4.0~4.4), and $Al_{13}Fe_4$. For the ones with cerium, it was possible that the cerium absorbed or went into the particles and formed some unknown ternary phases locally.

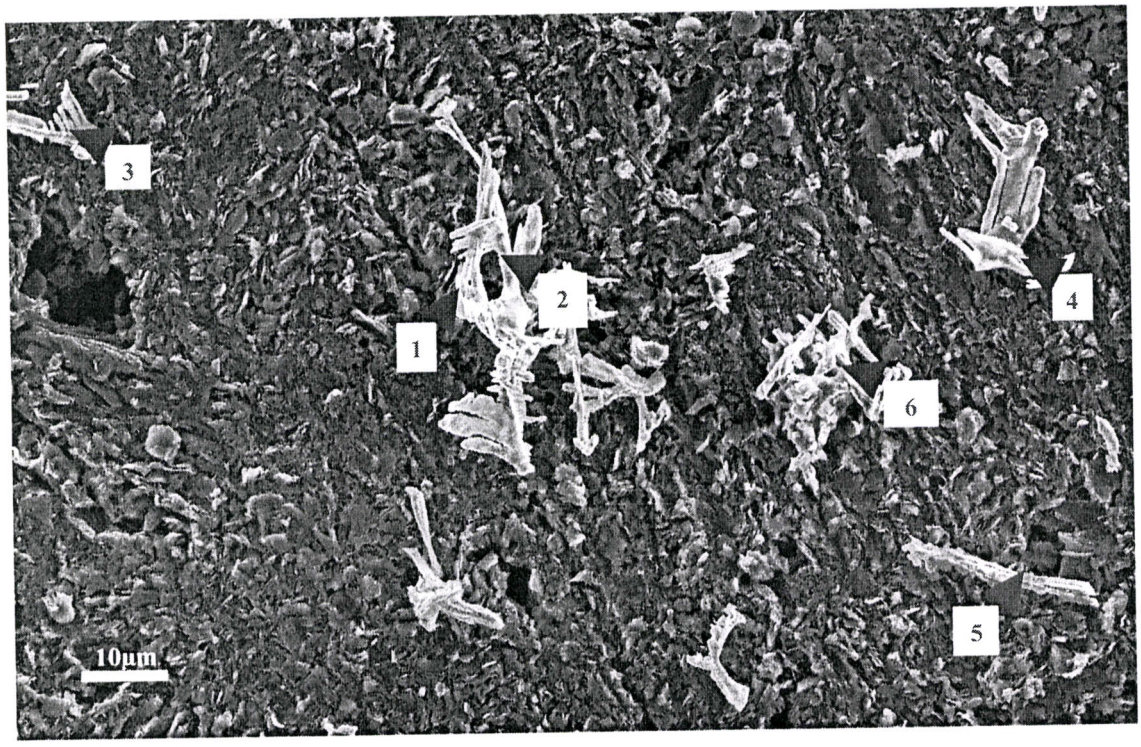

Figure 3.19 SEM picture of extracted intermetallics from as-cast 0.3Ce alloy on graphite disk at SE mode.

In Table 3.7, the composition of particle **1** and particle **6** indicated that, the cerium atoms could go into the Fe-rich phases.

Table 3.7 EDS semi-quantification of chemical compositions of the intermetallics (in atomic %)

Element / Point	Al	Fe	Ce	Approximate atomic ratio	Estimation of composition
1	73.2	17.3	4.77	15.3 : 3.6 : 1	Al_{15} ($Fe_{3.6}$, Ce)
2	51.6	14.5	—	3.6 : 1 : 0	Al_mFe
3	20.1	6.50	—	3.1 : 1 : 0	$Al_{13}Fe_4$
4	31.7	11.6	—	2.7 : 1 : 0	$Al_{13}Fe_4$
5	25.7	4.9	4. 4	5.8 : 1 : 1	Al_6Fe
6	29.7	5.0	7. 1	6.0 : 1: 1.4	Al_6(Fe, Ce)

A single particle is observed in Figure 3.20 and Figure 3.21. In contrast to the XRD analysis result, it seems that compositions of these binary Fe-rich phase particles are location-variant, cerium is detected at some points, as seen in Table 3.8 and Table 3.9. For the ternary phase of Al-Fe-Ce, instead of having the exact stoichiometric compositions shown on the phase diagram, predicted to be $Al_{10}Fe_2Ce$ (Ayer *et al.*, 1998) or Al_8CeFe_4 (Bus *et al.*, 1976) or the Al_8CeFe_2 phase (Yar. *et al.*, 1974) detected by XRD analysis, small variation of atomic ratios are indicated by XRD analysis. In

Figure 3.20, cerium was detected in the middle of the dendrite arms and some was at the dendrite tips. It seemed that, the cerium absorbed onto or diffused into the particles and formed a solid solution with the Al-Fe particles.

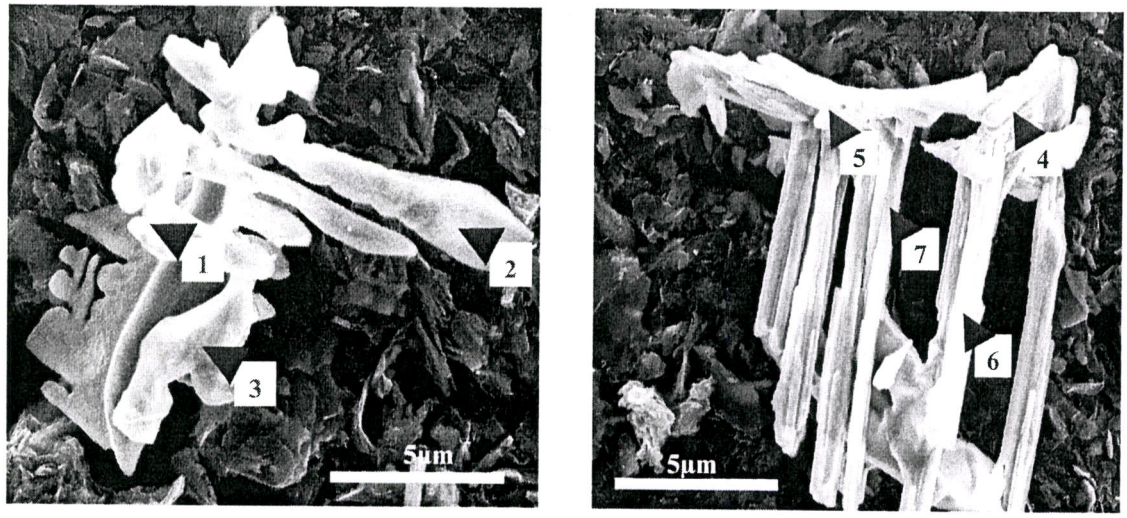

Figure 3.20 SEM pictures of extracted intermetallics from as-cast 0.3Ce alloy on graphite disk at SE mode.

Table 3.8 Semi-quantification of chemical compositions of the intermetallics in Figure 3.20 by EDS (in atomic %)

Element / Point	Al	Fe	Ce	Approximate atomic ratio	Rough Estimation of stoichiometric composition
1	14.9	4.6	1.2	12.5 : 4: 1	$Al_{12.5}(Fe_4, Ce)$
2	22.2	6.2	—	3.6 : 1 : 0	Al_mFe (m=4.0-4.4)
3	21.0	4.4	—	4.7 : 1 : 0	Al_mFe (m=4.0-4.4)
4	23.7	7.63	—	3.1 : 1 : 0	$Al_{13}Fe_4$
5	13.8	5.27	1.27	11 : 4.1 : 1	$Al_{11}(Fe_4, Ce)$
6	28.0	9.4	2. 7	10.3 : 3.5 : 1	$Al_{10.3}(Fe_{3.5}, Ce)$
7	53.0	15.2	4. 0	13 : 3.8 : 1	$Al_{10}(Fe_4, Ce)$

Particles in Figure 3.21 show the typical Chinese script structure of Fe-rich intermetallic compounds. In the left image of Figure 3.21 , a much smaller particle of few microns in diameter was detected, and the EDS analysis result indicates that some local point composition has the closest stoichiometry to the ternary phase $Al_{10}Fe_2Ce$.

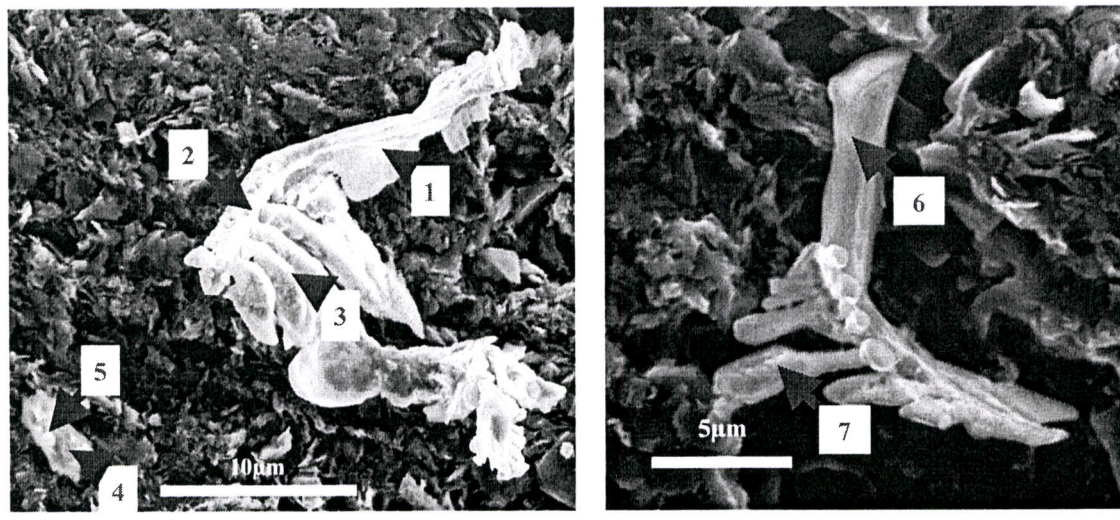

Figure 3.21 SEM pictures of extracted intermetallics from as-cast 0.3Ce alloy on graphite disk at SE mode

Table 3.9 Semi-quantification of chemical compositions of the intermetallics in Figure 3.21 by EDS (in atomic %)

Element / Point	Al	Fe	Ce	Approximate atomic ratio	Rough Estimation of stoichiometric composition
1	15.7	4.9	—	3.2 : 1 : 0	$Al_{13}Fe_4$
2	47.9	16.0	—	3 : 1 : 0	$Al_{13}Fe_4$
3	35.7	5.9	—	6.1 : 1 : 0	Al_6Fe
4	27.9	4.8	3. 0	9.4 : 1.6 : 1	$Al_{10}(Fe_2, Ce)$
5	27.5	7.9	2. 1	13 : 3.8 : 1	$Al_{13}(Fe_{3.7}, Ce)$
6	17.0	4.7	—	3.6 : 1 : 0	Al_mFe (m=4.0-4.4)
7	54.6	18.1	—	3.01 : 1 : 0	$Al_{13}Fe_4$

EDS semi-quantified the chemical atomic ratios of the intermetallic powders extracted from 0.3Ce alloy. The analysis results indicate that the exact compositions of phases were difficult to attain by XRD, and there are more unknown binary and ternary phases needed to be identified in other methods.

According to the stoichiometry listed in Table 3.7, Table 3.8 and Table 3.9, the phases possibly included in the 0.3Ce alloy were listed in Table 3.10,

Table 3.10 Major phase estimation in 0.3Ce alloy by EDS

Binary Ce-rich phase	Binary Fe-rich phase	Ternary Phase
Al_4Ce	Al_6Fe, Al_mFe, m=4-4.4, $Al_{13}Fe_4$	$Al_{10}(Fe_2, Ce)$, $Al_8(Fe_2, Ce)$, $Al_8(Fe_4, Ce)$

The morphology of a Fe-rich particle seemly can be influenced by the competition

between the anisotropic growth and the growth inhibition from cerium absorption. The particle size might be reduced if the cerium shield the particle from the melt and prevent Fe diffusion to the particle, as seen in Figure 3.21. Big dendrite particles are also observed, which indicated the insufficient morphology modification of cerium. It needs further quantification to see, to what extent, the small addition of cerium had changed the morphology of Fe-rich dendrites, e.g. particle aspect ratio, phase volume fraction. SEM/EDS is not sufficient to identify the cerium-containing phases. But variant local composition of particles confirm the interaction between cerium and Fe-rich particle.

3.6.4 TEM Results

Phase identification by TEM was performed by our project co-workers Professor David. Mitlin and Dr. Jian Chen from University of Alberta. Phases of Al_6Fe and Al_mFe (m=4.0-4.4) and unknown Fe-Al intermetallics were detected in the reference alloy, as seen in Figure 3.22-Figure 3.24 respectively.

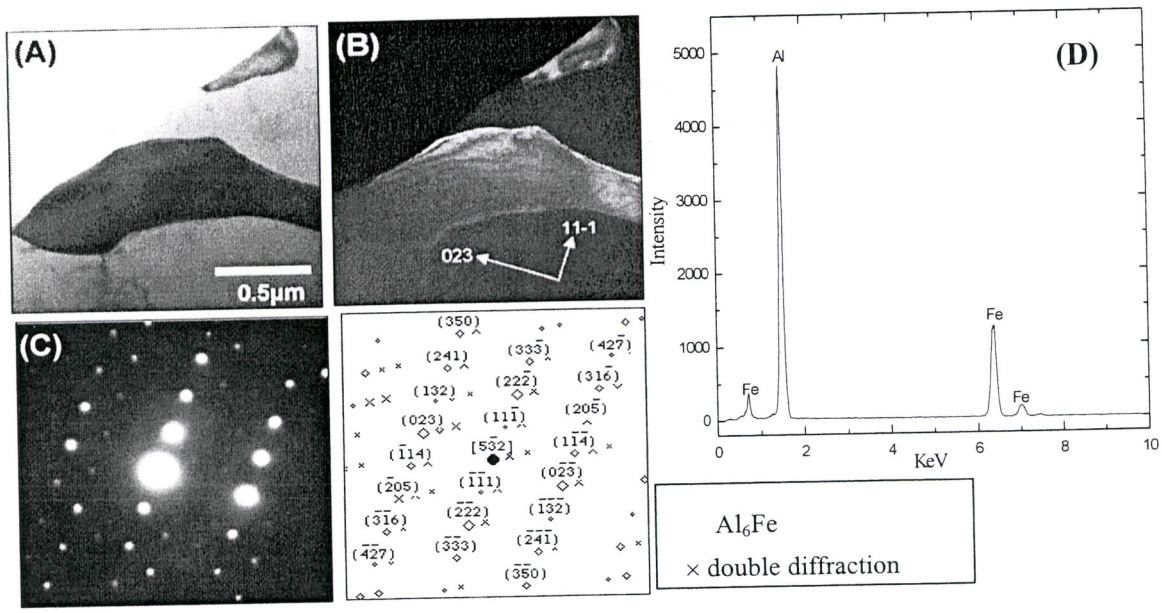

Figure 3.22 Transmission electron micrographs (A) and (B) are the bright field and dark field images of Al_6Fe by choosing (023) reflection as shown in (C) the selected electron diffraction pattern (SADP) and its simulation. (D) is the EDS of Al_6Fe in micrograph (A). (By Dr. Chen, Jian, University of Alberta)

The Al_mFe (m=4.0-4.4) phase was frequently observed in the Al matrix, and its TEM micrographs were shown in Figure 3.23. The Al_mFe crystal structure data for SADP simulation is from Gjønnes et al. (1998).

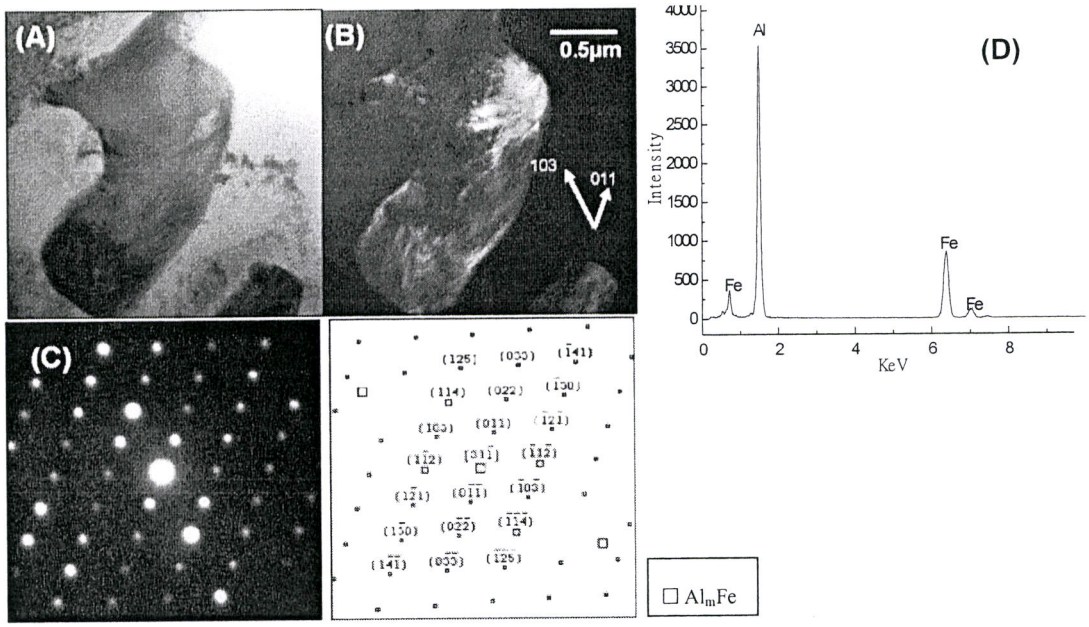

Figure 3.23 Transmission electron micrographs (A) the bright field and (B) dark field images of Al_mFe (m=4.0-4.4). (C) The corresponding SADP and its simulation. (D) the EDS profile of Al_mFe. (By Dr. Chen, Jian, University of Alberta)

An unknown Fe-Al intermetallic was detected by TEM in the Al matrix, as seen in Figure 3.24. The unidentified phase was suggested by EDS that its main content is iron.

In the reference alloy, the binary phases Al_6Fe and Al_mFe were observed by TEM, where Al_mFe appeared more frequently. This result was generally consistent with the XRD analysis and EDS results, except that the EDS analysis indicated the possible existence of $Al_{13}Fe_4$. In the XRD analysis result of reference alloy, only Al_mFe phase was identified as the dominated Fe-rich phase.

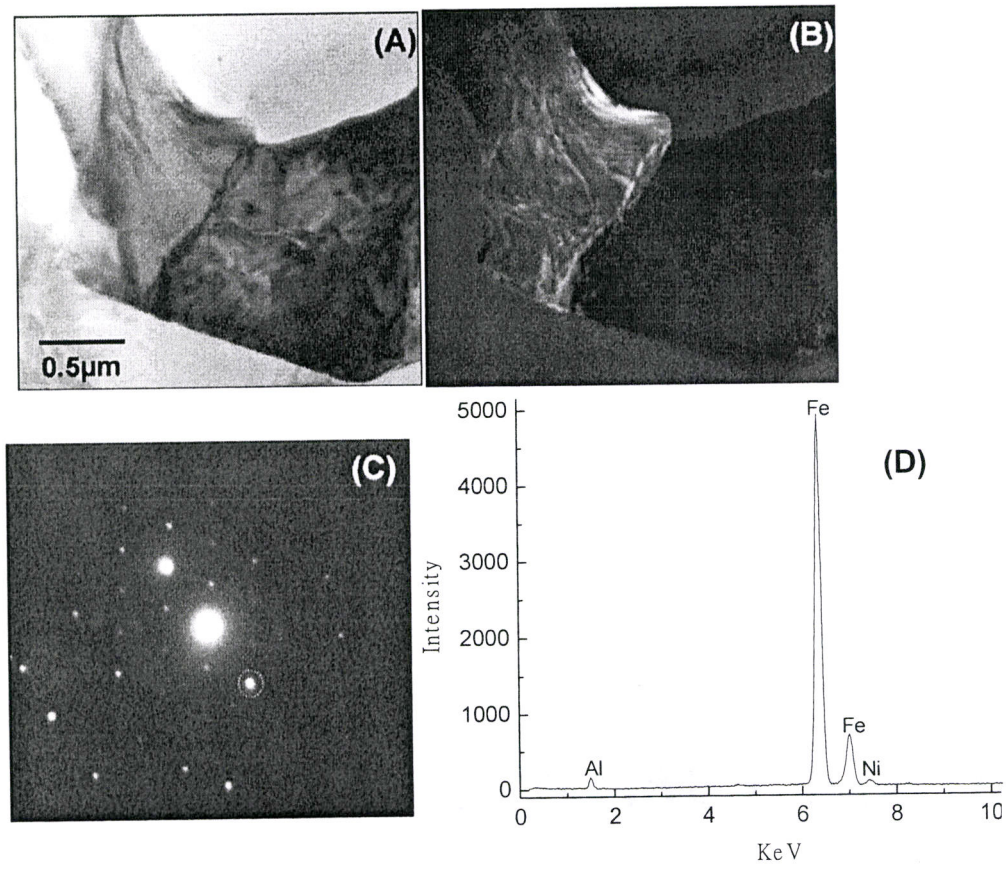

Figure 3.24 Transmission electron micrographs (A) the bright field images of unknown Fe-Al intermetallics. (B) dark field image obtained by choosing the circled reflection in the (C) SADP. (D) The corresponding EDS profile. (By Dr. Chen, Jian, University of Alberta)

In the 0.3Ce alloy, a binary cerium-containing phase was identified, as illustrated in Figure 3.25. As the information about the atom locations in Al_4Ce was not available, the simulation was conducted using the crystal structure data of Cu_5Li_7P, which has the same space group and atom arrangement to Al_4Ce. A ternary phase of Al_8CeFe_2 was also found in the 0.3Ce alloy, as seen in Figure 3.28. It was observed that these two cerium-containing phases were much smaller than the Al-Fe phases. With sizes of less

than one micron, these particles would easily be decanted during the particle extraction, and this explained why so little cerium-containing phases were detected in the 0.1Ce alloy in XRD test, and barely ones detected in EDS analysis section.

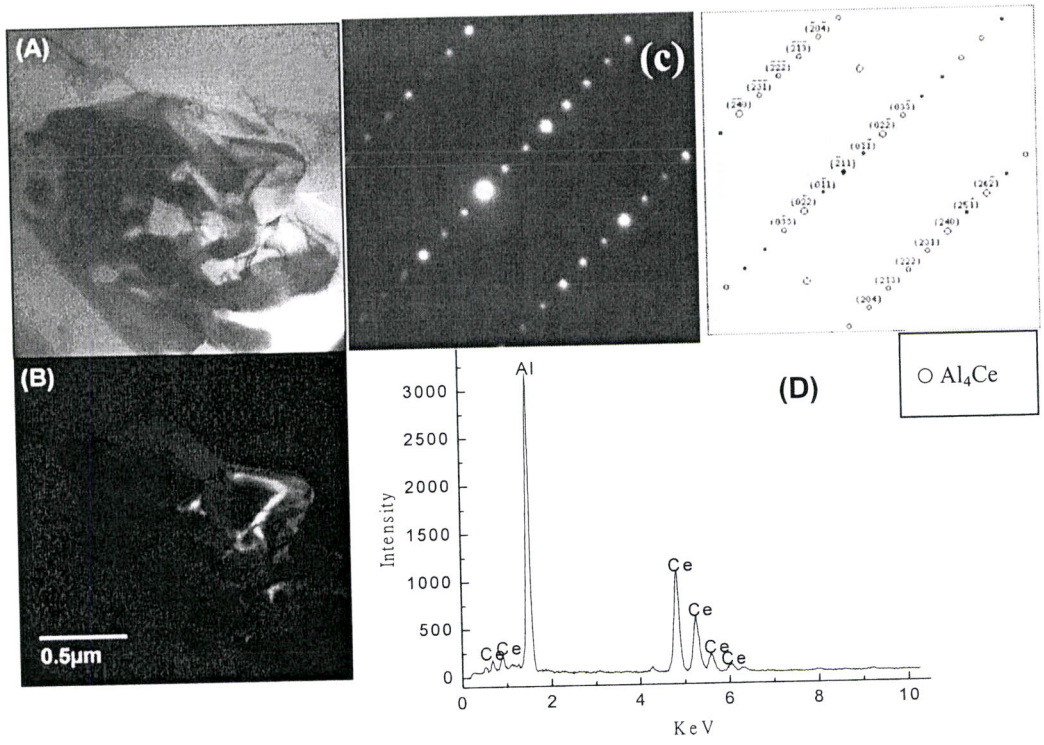

Figure 3.25 Transmission electron micrograph (A) displays the bright field of the precipitate cluster of certain intermetallic. (B) The dark field image was obtained by choosing g=-2-2-2 reflection. (C) The SADP and its simulation and (D) the EDS suggest the arrowed area is Al_4Ce. (By Dr. Chen, Jian, University of Alberta)

It was observed in TEM that, some of the Al_4Ce clustered together, and caused dislocations in the Al matrix (as seen Figure 3.26). This stress concentration was introduced in the local matrix. It might lead to early void initiation during deformation.

As showed in Figure 3.27, it was also found that the compositions of the particles in Figure 3.25 and Figure 3.26 were location-variant. Silicon was unexpected in random spots on these phases. As almost none such silicon-containing phase was detected in the XRD and EDS analysis, it indicated that, a tiny amount of silicon could form few intermetallic compounds with Al, Mg and Ce. However, this EDS was done without quantification, so the compositions of these compounds were still unknown. However, it might indicate that, the cerium could remove the silicon from Al matrix by forming some fine particles, and this could be related to the cluster formation.

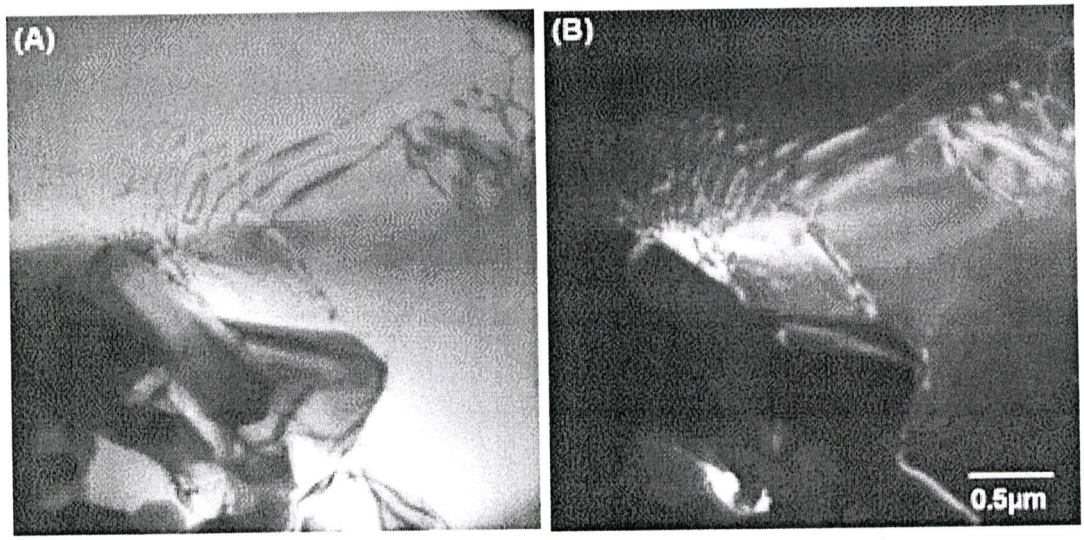

Figure 3.26 Transmission electron micrograph (A) the bright field and (B) the dark field image of the dislocation within aluminium matrix, which is close to Al_4Ce clusters. (By Chen, Jian from University of Alberta)

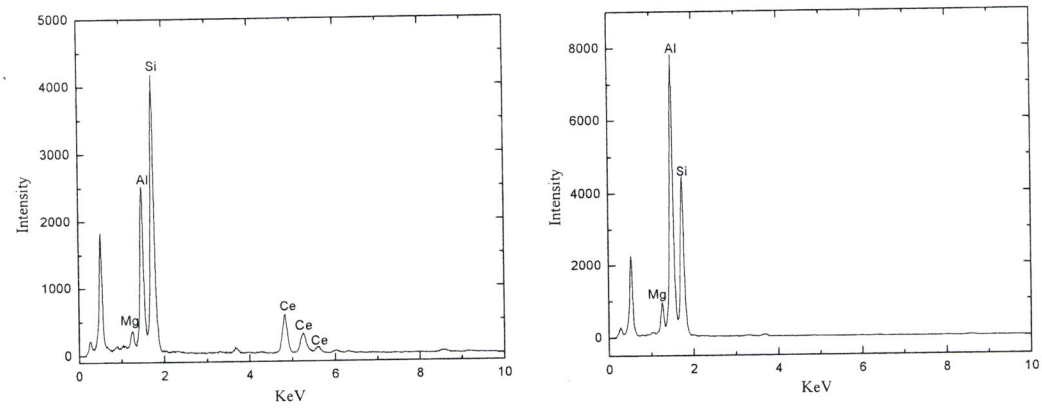

Figure 3.27 EDS profiles of random spots on the cluster particles of Al_4Ce phase. (By Dr. Chen, Jian, University of Alberta)

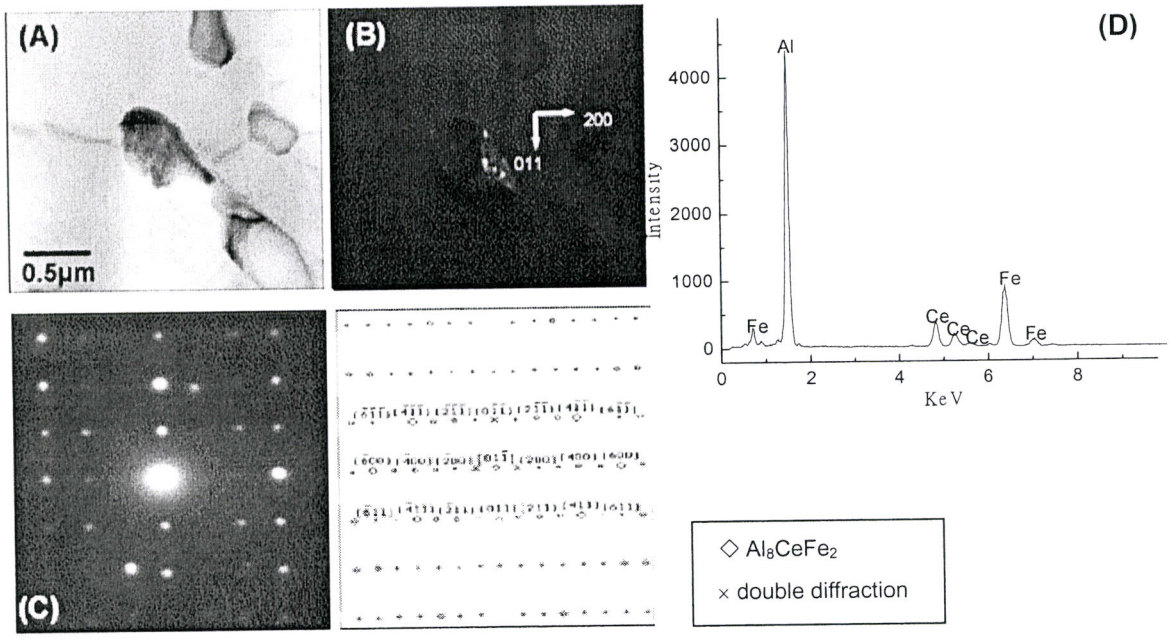

Figure 3.28 Transmission electron micrograph (A) the bright field image of Al_8CeFe_2 phase. (B) The corresponding dark field image obtained by choosing g= 411 reflection (C) The corresponding SADP and its simulation. (D) EDS profile of the phase. (By Dr. Chen, Jian, University of Alberta)

Summarizing the phase identification results from XRD, EDS and TEM, it can be concluded that, the addition of cerium forms fine intermetallic phases with elements of Al and Fe in the Al matrix, or absorbing on the big Al-Fe dendrites. The coarse Al-Fe phase still is the major intermetallic phases for the AA5754 alloys. Therefore, the phases detected by XRD, EDS and TEM were summarized in Table 3.11.

Table 3.11 Major phase identification of the intermetallics in reference and 0.1Ce and 0.3Ce alloys

	XRD	EDS (semi-quantification)	TEM
Reference	1. Al_mFe (m=4-4.4)	Not analyzed	**Major phase** 1. Al_mFe 2. Al_6Fe
			Unknown phase 1. Fe-Al intermetallics
0.1Ce	**Major phase** 1. AlmFe (m=4-4.4) 2. Al_4Ce	Not analyzed	
	Minor phase 1. Al_8CeFe_2		
	Unknown phases		
0.3 Ce	**Major phase** 1. AlmFe (m=4-4.4) 2. Al_6Fe 3. Al_4Ce	**Major phase** 1. Al_6Fe 2. Al_mFe (m=4-4.4) 3. $Al_{13}Fe_4$	**Major phase** 1. Al_mFe (m=4.0-4.4) 2. Al_6Fe 3. Al_4Ce Few are silicon containing
	Minor phase 1. Al_8CeFe_2 2. $Al_{92}Ce$	**Minor phase** 1. Al_{10}(Fe_2, Ce) 2. Al_8(Fe_2, Ce)	**Minor phase** 1. Al_8CeFe_2
	Unknown phases	3.Al_8(Fe_4, Ce)	

3.7 Artificial Aging and Macrohardness Test

Artificial aging samples for macrohardness tests were prepared from the quenched reference and 0.3Ce sheet alloys, which had been 60% reduction cold-rolled and fully annealed. For each composition alloy, 6 samples were heated at 170 °C for 4, 6, 8, 12, 18 hours respectively. All of them were water quenched and ready for macrohardness test.

Rockwell B scale is generally applied to testing precipitation hardened Al alloys. With the 100kg load, each annealed and water-quenched sample surface was indented with 1/16" steel ball at 15 various points, which were 1cm away from edges. Average hardness and its corresponding standard deviations (error bars) was recorded.

Rockwell hardness testing results are presented in Figure 3.29. Neither the reference alloy nor the 0.3Ce alloy showed any measurable hardening effect. The largest variation of R_B value was within 3 HRB in the 0.3Ce alloy. And the difference of hardness between reference alloy and 0.3Ce alloy was no larger than 9 HRB. It can be concluded that, although the addition of cerium increased the hardness of Al-Mg-Fe slightly, there was no detectable strengthening happened during the aging. Since the grain structures of the two rolled and annealed alloys were similar, this slight increase could be attributed to the extra cerium-containing particles. A wavy descendent curve of hardness

was observed in each alloy. This is due to the diffusion and growth of the intermetallics during long time of aging. The total number of intermetallic particles was reduced as their sizes increased. The spacing between these particles became larger, which lead to the decrease of the alloy hardness.

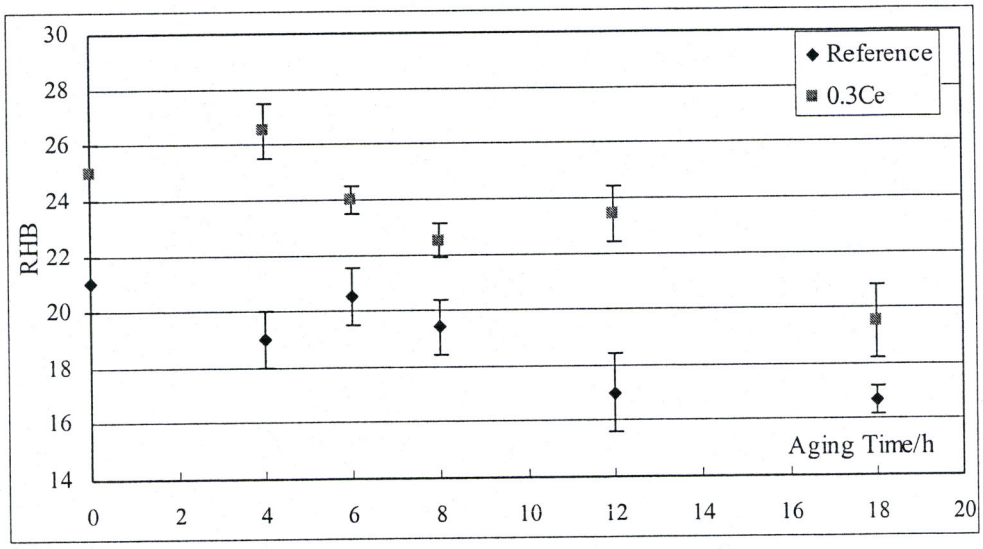

Figure 3.29 Rockwell hardness of reference alloy and 0.3Ce alloy aged for different time

Rockwell hardness of reference alloy and 0.3Ce alloy, which had only been homogenized for 4 hours, was 17.5±1.5 R_B and 23±1 R_B respectively. Comparing with the data of aged samples, it can be concluded that the thermo-mechanical processing generates negligible enhancement on the alloy hardness.

Thus, no precipitation hardening happened to the cerium-doped Al-Mg-Fe alloy during the heat treatments. The cerium-doped Al-Mg-Fe alloy is still non-heat-treatable.

3.8 Uniaxial Tensile Test

3.8.1 Tensile Specimen Preparation

Effect of cerium additions on the mechanical properties of this simplified AA5754 alloy were tested by uniaxial tensile testing. Specimens were prepared from the as-cast, fully annealed 60% reduction and 90% reduction alloy pieces for each of the reference, 0.1Ce and 0.3Ce alloys. Tensile specimens for as-cast alloys and thermo-mechanically processed alloys were sectioned at the directions shown in Figure 3.30, where CD stands for the casting direction of ingots, RD stands for the rolling direction and TD stands for the transverse direction.

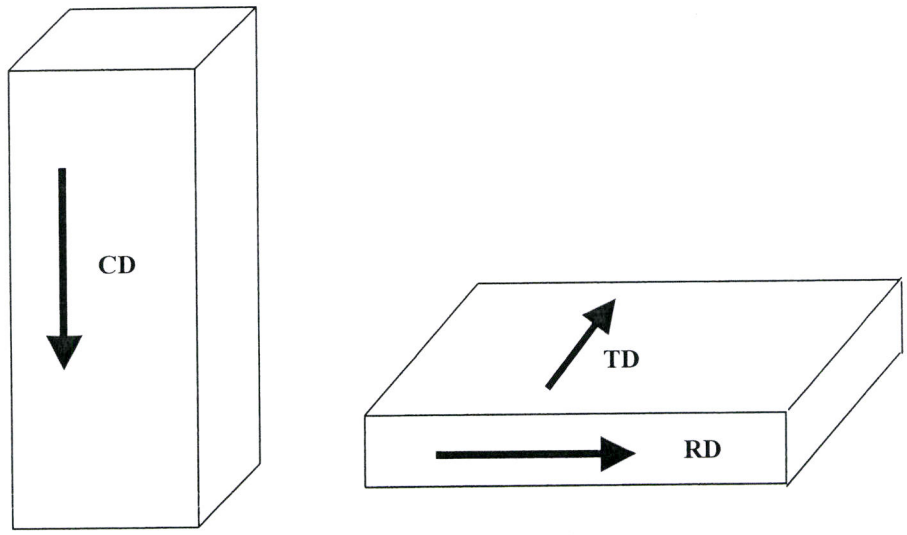

Figure 3.30 The section direction of specimens from as-cast and rolled alloys

The specimen dimensions are illustrated in Figure 3.31. All the tension tests were performed at room temperature. With an initial strain rate of 6×10^{-4} s^{-1}, the material was pulled at a crosshead speed of 0.45 mm/min.

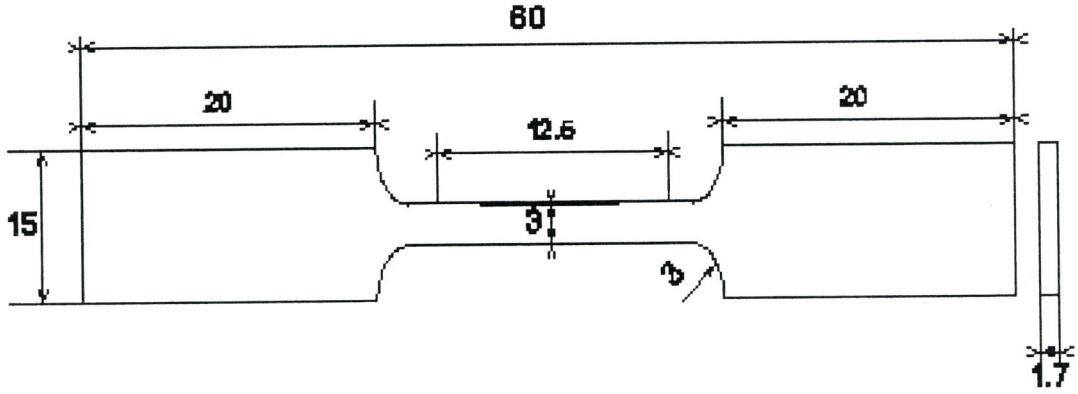

Figure 3.31 Rectangular tension test specimens (in mm)

3.8.2 Tensile Stress-Strain Diagrams

A tensile profile of the material's reaction to the pulling force was obtained by tension test. From the stress-strain curve, ultimate tensile strength (UTS) and its uniform elongation was recorded to evaluate the specimen's strength and prior-necking ductility respectively. It was found that, the strength of the alloys was generally enhanced by the thermo-mechanical processing, while the prior-necking ductility remains the same.

For example, the tensile behaviors of one as-cast 0.1Ce alloy sample and corresponding cold-rolled and annealed 0.1Ce samples sectioned at RD were presented in Figure 3.32. The UTS of the alloy went up almost 20 MPa after the 60% cold-rolling and fully annealing, while its uniform elongation slightly increased by around 0.03. The true strain-stress curves of the 60% and 90% rolled and annealed samples almost overlapped each other, neither the UTS nor the uniform elongation further went up in the corresponding 90% cold-rolled and annealed 0.1Ce sample.

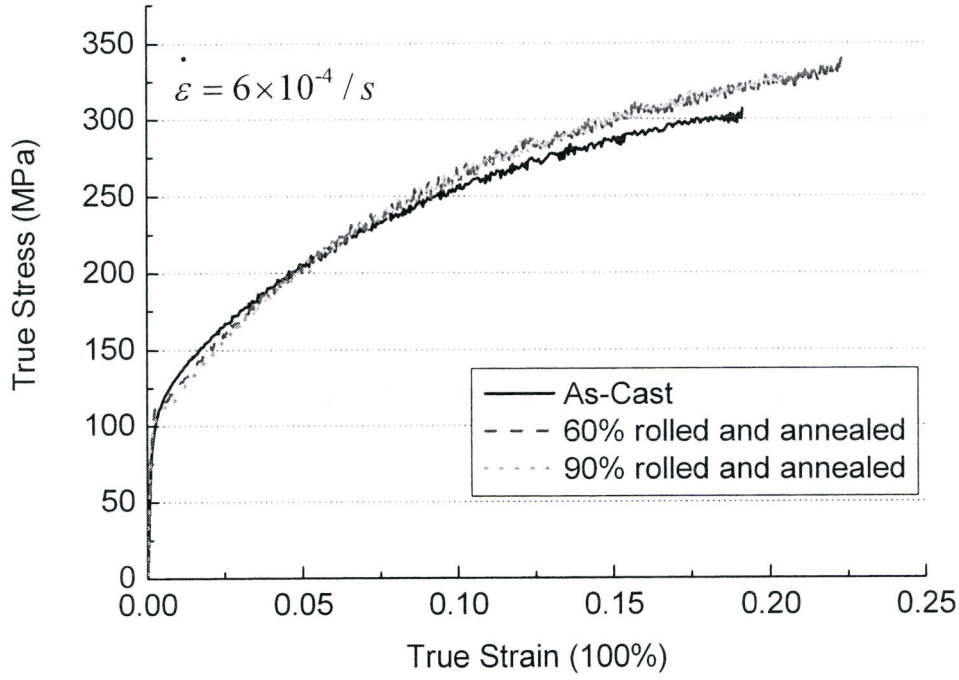

Figure 3.32 True stress-strain curves of 0.1Ce alloys sectioned at casting direction and rolling direction.

Al-Mg-Fe alloy tensile test results of AC specimens and RD specimens are presented in Table 3.12 and Table 3.13. For each alloy parameter, the average value and corresponding standard variance were gained from 6 identical samples. It was found that the slight increase in ductility can be neglected as it was within the range of errors, and the thermo-mechanical processing had no influence on the uniform elongation of the 0.1Ce alloys.

Table 3.12 Tension test results of as-cast specimens at CD

Alloy	UTS (MPa)	Uniform elongation
Reference	228±1	0.21±0.02
0.1Ce	253±2	0.21±0.02
0.3Ce	236±2	0.22±0.01

Table 3.13 Tension test results of cold-rolled and annealed specimens at RD

Alloy	Reduction during cold rolling	UTS (MPa)	Uniform elongation
Reference	60%	266±4	0.21±0.02
	90%	265±6	0.24±0.01
0.1Ce	60%	272±3	0.24±0.01
	90%	271±2	0.23±0.01
0.3Ce	60%	269±5	0.21±0.01
	90%	270±4	0.23±0.01

Similar trend was found in the reference and 0.3Ce alloys. No measurable increase was observed in uniform elongation. The UTS of the alloys were enhanced by the thermo-mechanical processing. It is known that, Al-Mg alloy is a work-hardenable alloy. However, as it was fully annealed, the extra strength gained through further deformation was lost during full annealing. Therefore, there was no further strengthening in the 90% cold-rolled and annealed alloys.

Due to the strengthening effect of cerium addition to the as-cast alloys, the UTS of AL-Mg-Fe alloy was increased by about 25MPa in the 0.1Ce alloy, as shown in Figure

3.33. The UTS did not continue going up in the 0.3Ce alloy, but decreased a little. Up to now, the 0.1 wt.% was the optimal amount of addition for as-cast Al-Mg-Fe alloy strengthening.

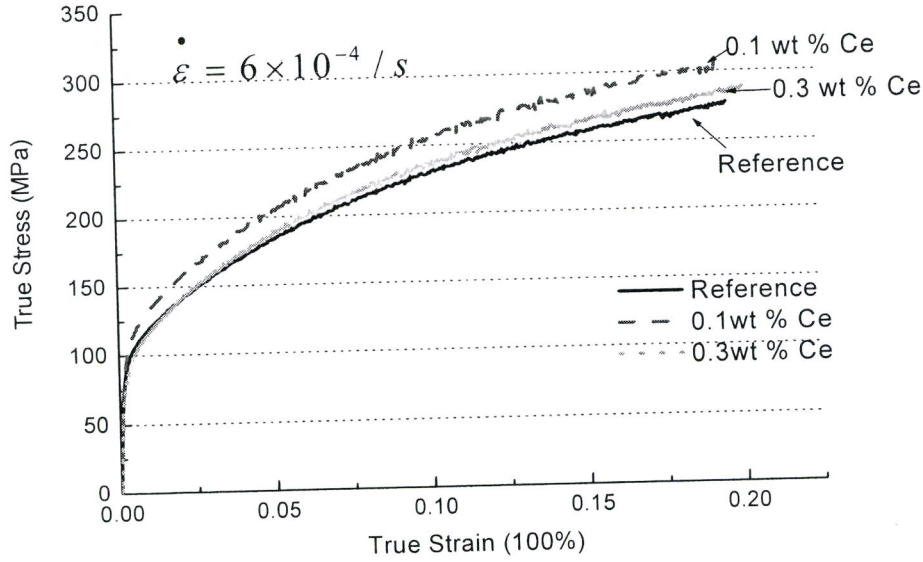

Figure 3.33 True stress-strain curves of as-cast alloys

The tensile test results of TD specimens are presented in Table 3.14. No measurable increase in UTS and uniform elongation was observed between the 60% rolled and 90% rolled alloys. Compared with the results in Table 3.12 and Table 3.13, it was noticed that, the UTS of the TD specimen was lower than its corresponding RD specimen, but higher than the as-cast one. For example, as shown in Figure 3.34, the

stress-strain curve of the RD specimen tops the TD one, and the TD curve is above the as-cast one. Therefore, the AA5754 alloys showed anisotropic tensile behaviors.

Although a slight increase in the uniform elongation was observed in the profile, it should be neglected as it was within the error range. Moreover, the elongation in TD specimen was close to that in corresponding RD specimen. Therefore, the prior-ductility of Al-Mg-Fe alloy is isotropic.

Table 3.14 Tension test results of cold-rolled and annealed specimens at TD

Alloy	Reduction during cold rolling	UTS (MPa)	Uniform elongation
Reference	60%	247±6	0.20±0.03
	90%	245±3	0.22±0.01
0.1Ce	60%	259±2	0.23±0.01
	90%	264±2	0.25±0.02
0.3Ce	60%	254±3	0.23±0.01
	90%	255±4	0.21±0.01

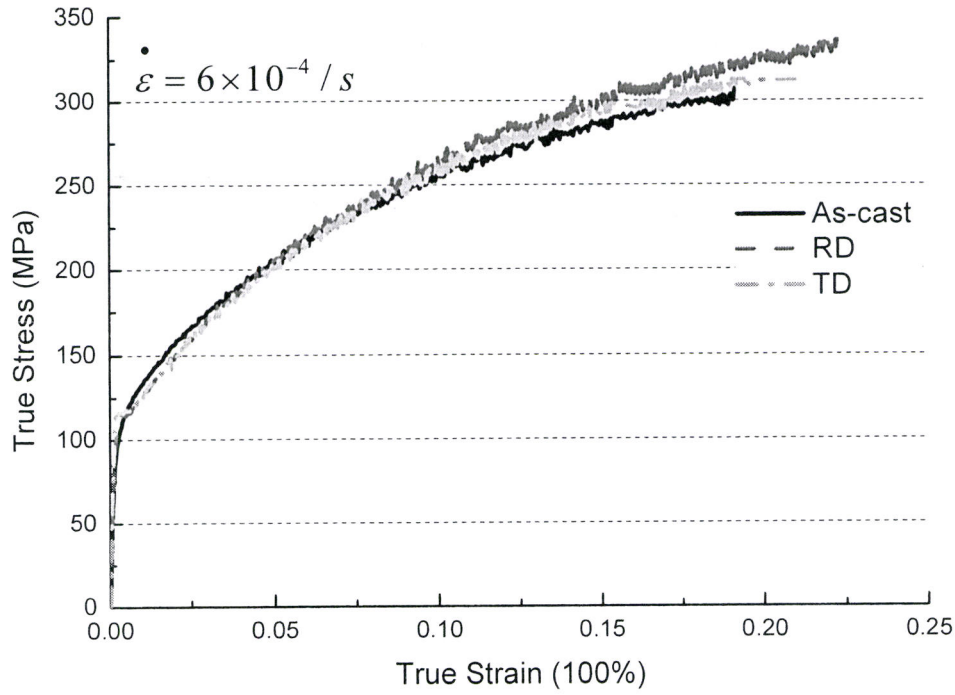

Figure 3.34 True strain-stress curves of as-cast, 60% cold-rolled and annealed RD and 60% cold-rolled and annealed TD specimens of the 0.1Ce alloy

As shown in Figure 3.35 and Figure 3.36, the stress-strain curves of these cold-rolled and annealed reference, 0.1Ce and 0.3Ce alloys almost overlapped each other. The strengthening effect of cerium on the as-cast alloy has been eliminated by the work-hardening provided by the thermomechanical processing.

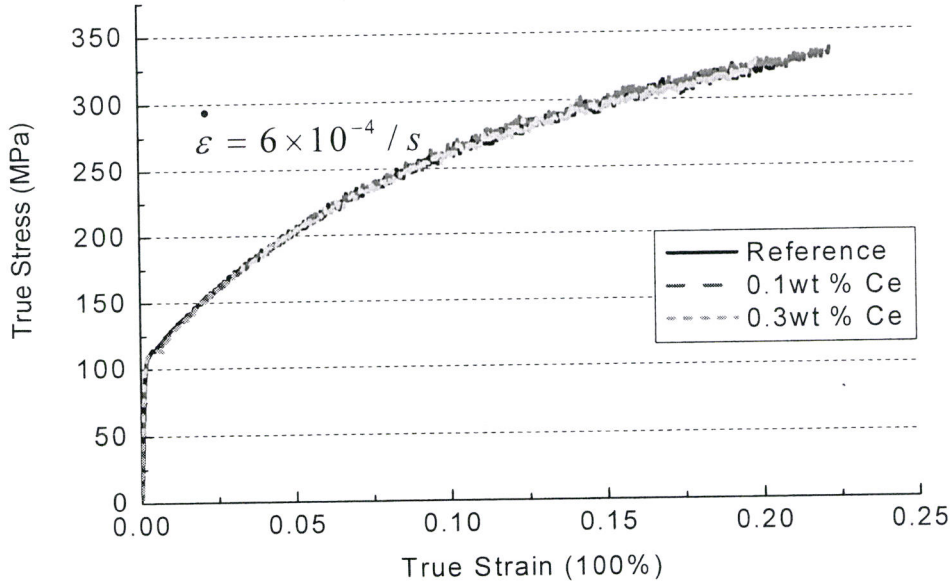

Figure 3.35 True stress-strain curves of 60% cold rolled and annealed Alloys (at RD)

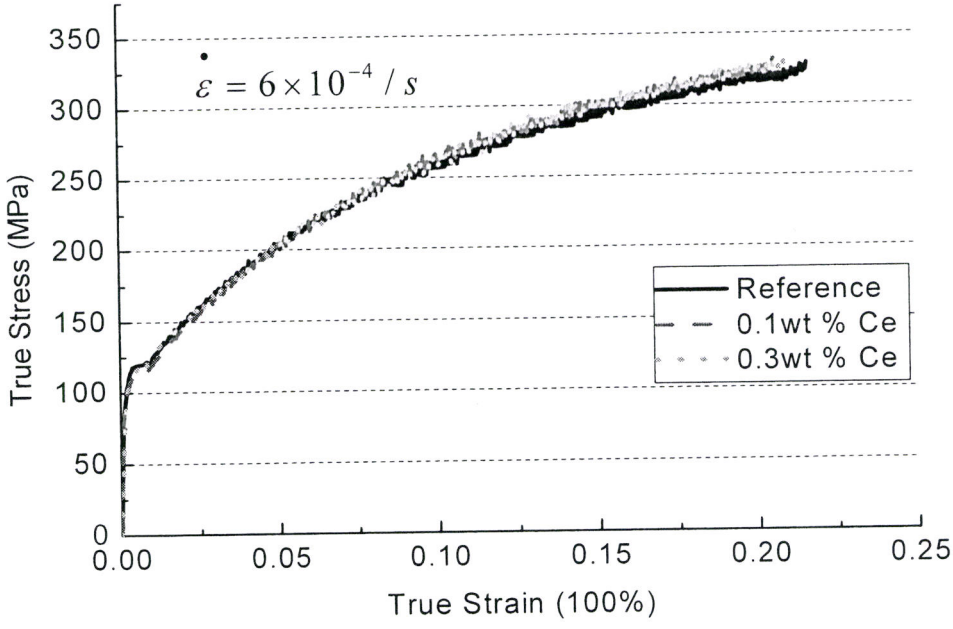

Figure 3.36 True stress-strain curves of 90% cold rolled and annealed alloys (at RD)

The modification effect of cerium addition on the TD specimen had not been completely eliminated by the thermo-mechanical processing. As shown in Table 3.14, the UTS of 0.1 Ce alloy was still higher than the reference alloy by around 10 MPa.

In conclusion, both the thermo-mechanical processing and addition of cerium increased the strength of the as-cast Al-Mg-Fe alloy. But the advantage of cerium-doped alloy was eliminated when alloys went through thermo-mechanical processing. The anisotropic strength of cold-rolled and annealed alloys was higher at RD than at TD. The prior-necking ductility of the alloy is isotropic.

3.8.3 Reduction Areas and Fracture Strains

Pictures were taken of the fracture surface of tension specimens by the stereo microscopy connected with a digital camera. The reduction in area of the fracture surface was then measured with calibration by the Eclipse Version 6.0 image analysis as well. The projection area towards the transverse section plane was measured as the final fracture area, which was described as in Figure 3.37.

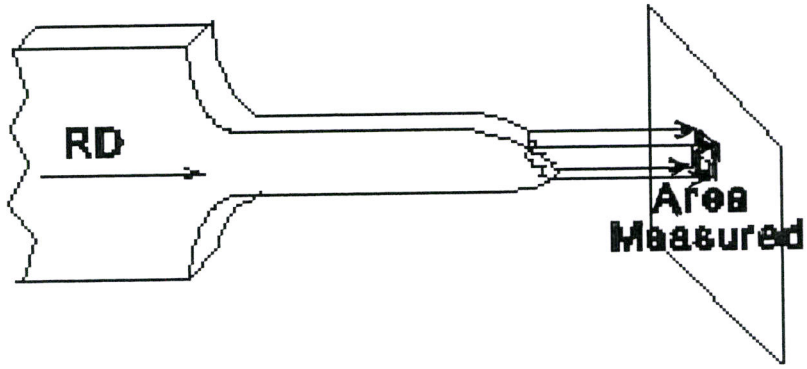

Figure 3.37 Final fracture area measurement

The reduction in area (RA) at fracture was measured as an estimation of the general ductility of the alloy. By Datsko and Yang (1960)'s empirical equation $\frac{R_{\min}}{t} = \frac{C}{RA} - 1$, the measured RA could be used as a rough indication of the alloy bendability. The reduction in area is $RA = 1 - \frac{A_f}{A_0}$, where A_f is the measured final area, and A_0 is the initial area measured at the middle of the specimen. The true fracture strain $\varepsilon_f = \ln \frac{A_0}{A_f}$ is also an important parameter for material ductility.

Each sample fracture surface was measured 5 times, and the results were given in Table 3.15 and Table 3.16. No measurable increase of the reduction area and fracture strain was observed in as-cast alloys with Ce addition.

Table 3.15 Tension test results of as-cast specimens

Alloy	Reduction area (RA)	Average fracture strain (ε_f)
Reference	0.36±0.01	0.45
0.1Ce	0.35±0.02	0.43
0.3Ce	0.36±0.02	0.45

For the RD specimens of the cold-rolled and annealed the alloy, it was found that, as presented in Table 3.16, the RA and hence fracture strain was enhanced comparing to the as-cast alloys. Therefore, the Al-Mg-Fe alloy ductility at RD was increased during thermo-mechanical processing. The more the alloy was reduced, the better ductility it gained. For different composition alloy that had gone through same thermo-mechanical processing, no measurable difference was observed in their RA and ε_f.

Table 3.16 Tension test results of cold rolled and annealed specimens at RD

Alloy	Reduction during cold rolling	Reduction Area (RA)	Average fracture strain
Reference	60%	0.41±0.01	0.53
	90%	0.53±0.01	0.76
0.1Ce	60%	0.43±0.01	0.56
	90%	0.51±0.01	0.71
0.3Ce	60%	0.44±0.01	0.58
	90%	0.53±0.01	0.76

The measurements of TD specimens of the cold-rolled and annealed the alloys were presented in Table 3.17. Similar to the specimens at RD, increase in the RA and ε_f was observed for the further reduced TD specimens. In comparison with the RD samples, the RA and ε_f of the TD specimens was much lower than that of the RD ones. Some of them were even lower that of the as-cast alloys. The ductility of these Al-Mg-Fe sheet alloys is anisotropic.

Table 3.17 Tension test results of cold rolled and annealed specimens at TD

Alloy	Reduction during cold rolling	Reduction Area	Average Fracture Strain
Reference	60%	0.32±0.02	0.39
	90%	0.49±0.01	0.67
0.1Ce	60%	0.33±0.01	0.40
	90%	0.49±0.01	0.67
0.3Ce	60%	0.40±0.02	0.51
	90%	0.47±0.01	0.64

In conclusion, the addition of cerium had no measurable effect on the ductility of the AA5754 alloy. The alloy ductility of Al-Mg-Fe sheet alloys at rolling direction was larger than at transverse direction. In general, the more reduction of the sheet alloy had been through, the better ductility it gained. With Datsko and Yang's equation, it can be predicated that, similar trend will be observed in alloy bendability.

4 DISCUSSION

4.1 Cerium Effect on the Microstructure of Al-Mg-Fe Alloy

4.1.1 Phase Identification of the Intermetallics in the Al-Mg-Fe alloys

Phase identification results from XRD, EDS and TEM indicated that Fe-rich phases dominate the second phase constituents in the Al-Mg-Fe alloys. At fast cooling rate, the Fe-rich phases mainly formed metastable Al_mFe (m=4.0-4.4) phases. Cerium-containing phases were identified both by XRD and TEM. Similar to the prediction result calculated by Thermo-Calc, Al_4Ce was the major cerium-containing phase in the Ce-doped as-cast alloy, little $Al_{92}Ce_8$ also formed in the 0.3 wt.% Ce alloy. It is noticed that while little Al_6Fe form in the reference alloy, significant amount of Al_6Fe phase was detected in the 0.3Ce alloy. The addition of cerium made the solid solution becomes more saturated, the solubility of iron in Al matrix decreased. The addition of cerium promotes more iron precipitating from the Al matrix and hence more Fe-containing phase formed, especially the Al_6Fe phases. However, among these observed phases, only $Al_{13}Fe_4$ and $Al_{11}Ce_3$ were reported according to the thermodynamic calculation. Besides, an unknown Fe-Al intermetallic particle was observed in reference alloy. Comparing these prediction and experimental results, we can see that metastable and some minor and non-binary phases cannot be predicted by Thermodynamic

modeling.

Among the possible ternary phases, only Al_8CeFe_2 was detected by XRD and TEM. It is shown that this phase had much smaller size than the Fe-rich binary phase. Because of their small dimensions, many of them would not be resolved by optical or scanning electron microscopy and unable to be detected by SEM and EDS. They could also be decanted away during intermetallic extraction. Therefore, great loss of this phase led to the bare detection of this ternary phase in XRD and TEM. It is still possible that other ternary phases, which are also hardly detectable, may form in the cerium-added alloys. Further work needs to be done to search for all the possible ternary phases in the alloy using TEM.

As shown in Figure 4.1, three new peaks were observed in the 0.1Ce and 0.3Ce alloys. The RIR (Reflective Intensity Ratio) of Al_mFe was reduced by the addition of cerium. The intensity of the peak of a phase is related to its fraction in the intermetallic powders. From the change of intensities of phases in the three profiles, it can be concluded that, while the Fe-rich phase fraction was reduced, there was a significant increase in the cerium-contained phase. As shown in Figure 4.1, the peaks at 29 degree were identified as Al_4Ce phases. However, the peak at 22 and 34 degrees were

unidentified. These phases appeared in the 0.1Ce alloy and became significantly stronger in the 0.3Ce alloy. In the 0.3Ce alloy, the peaks of the unidentified phases were greatly increased. Due to the fact that addition of alloying elements would influence each other's solubility, it is thought that the addition of cerium would not only form cerium-containing phases in the alloy, but also promote the precipitation of other alloying elements, e.g. Fe, by reducing their solubility in the Al matrix. The unidentified peaks could represent Al-Fe or Al-Fe-Ce or quaternary phases that have not been presented in literature.

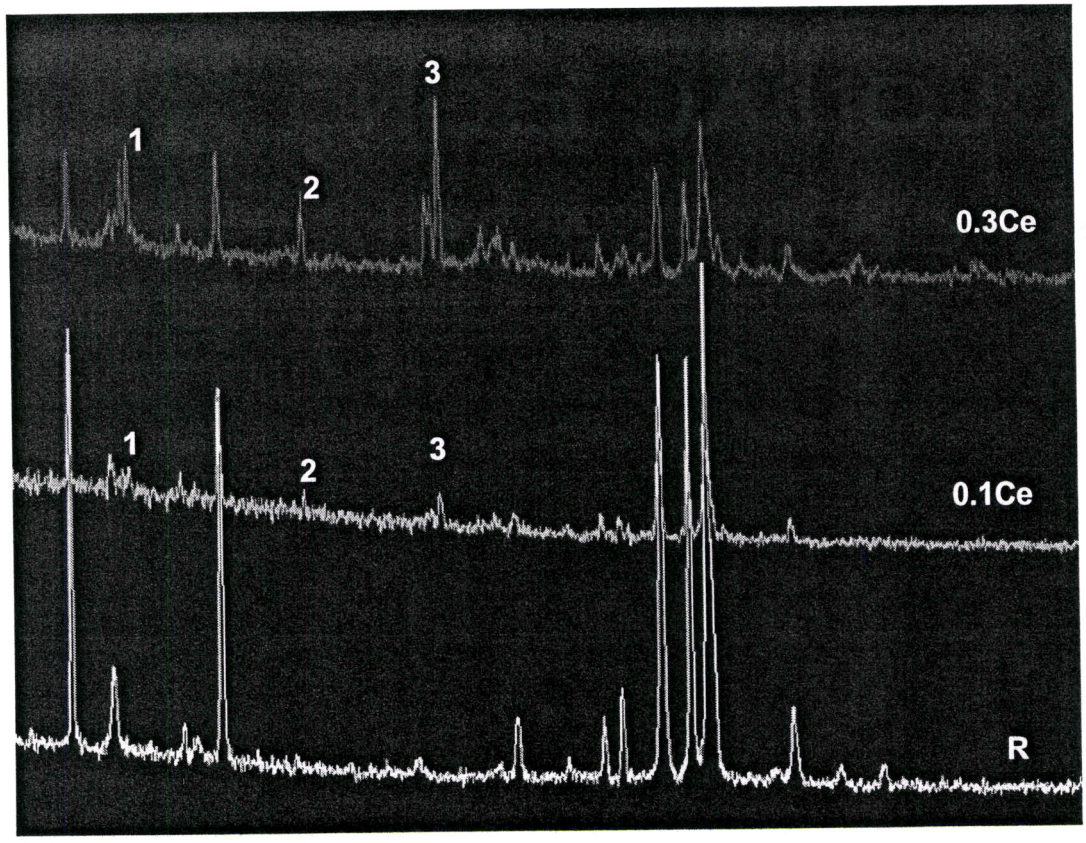

Figure 4.1 X-ray Diffraction profiles of extracted particle powders of Reference, 0.1Ce, 0.3Ce alloys (Peak 1 at 22 degree and peak 3 at 34 degree represents unknown phases, peak 2 at 29 degree represents Al_4Ce).

The interaction volume of X-rays was usually larger than the particle. The signal from aluminum matrix background would overlap with that of the particles, and thus make it impossible to get the actual chemical composition of intermetallic from the Al matrix. After extracting the particles and spreading them on the graphite disk, as the intermetallics studied were all carbon-free, the atomic ratio of each element could be calculated by just removing carbon signal, and thus the chemical composition of each particle could be estimated. Since EDS offers semi-quantification method of phase identification, all the stoichiometry was estimated and the ratios varied for a same phase. However, the semi-quantitative EDS was used to correlate the phase chemical composition estimation and morphologies. From its analysis results, the elongated phase or Chinese script phase was Fe-rich phases, while Al_4Ce was generally fine spheroids.

By this semi-quantitative analysis, it was confirmed that most of the particles were Al_mFe and Al_6Fe in the Al-Mg-Fe alloys. In the cerium-doped alloys, Al_4Ce and tiny amount of ternary phase Al_8CeFe_2 exist. During the EDS analysis on extracted intermetallic particles from 0.3Ce alloy, it was found that the chemical composition of a single particle, e.g., a Chinese script particle, was location-variant. Cerium was detected on some spots while not on the others. It seemed that cerium absorbed onto the surface of the big Fe-rich particle, or even diffused into it. This situation is quite similar to the one

in Sr-added Al-Fe-Si alloy. Since measurable decrease in particle size and aspect ratio was observed in cerium-doped alloy, It could be supposed that the cerium shielded the particle from melt by absorption onto the particle, and hence inhibited its further growth; or cerium diffused into the Fe-rich phase, decomposed the phase and formed smaller intermetallic particles. However, these two mechanisms do not promise that all Fe-rich particles would be modified. Cerium-containing big Fe-rich dendrites still existed in the alloy. Therefore, the phase morphology transformation is a process of competition between cerium modification and particle anisotropic growth.

At a small content level, the effect of cerium on Fe-rich dendrite is not as strong as Sr on Al-Fe-Si particles. The Sr inhibited the transformation from Chinese script α phase to needle-like β phase. However, in the simplified AA5754 alloy, due to the lack of silicon and fast cooling rate, most of the Fe-containing phases formed in Chinese script. It is probably that, for such less detrimental phase, the modification effect of cerium is limited inherently.

In TEM, some cluster of Al_4Ce particles with dimensions around few microns were observed in the 0.3Ce alloy. The compositions of these particles are also location-variant. Stress concentration was introduced in the Al matrix around them. The

little amount of silicon that had been detected randomly inside these particles might be related to the formation of such clusters. Bath (1912) mentioned that silicon would be removed by cerium by forming cerium silicide. Here it seemed that the cerium did have good affinity with silicon. However, due to its negligible amount, no extensive cerium silicide would form and lead to precipitation hardening to the cerium-doped Al-Mg-Fe alloy.

It was found that almost all of the Fe-containing or cerium-containing extracted intermetallic particles were magnesium-free. This indicated that, the addition of cerium did not result in increased precipitation of magnesium, as it did to iron. However, besides Al_3Mg_2, negligible Mg_2Si was detected in the three composition alloys. Therefore, little silicon was still inevitably introduced as impurity to the Al-Mg-Fe alloys.

The results of XRD and EDS and TEM basically identified the same major phases in the simplified AA5754 alloys. However, without absolute values of the number of each phase particles, it was unknown, to what extents, the addition of cerium had influenced the volume fraction of Fe-rich phases.

4.1.2 The Morphology and Volume Fraction of Intermetallic Particles in As-Cast Alloys

The Fe-rich phase was observed mainly in two morphologies in the as-cast Al-Mg-Fe reference alloy-Chinese script (aluminide dendrite) and needles. These particles of several microns in length had very low aspect ratio, less than 0.2. After addition of cerium, the Fe-rich phases became thicker and shorter. In Figure 4.2, the isolated coarse particles formed in the reference alloy, while the fine but closely-located intermetallic particles formed in the cerium-containing alloys. Phase identification results indicated that most of the phases in the cerium-containing alloys were still Al-Fe phases. Therefore, as mentioned previously, the addition of cerium has effect on the morphology of Fe-rich phases, it also seemed that the formed Al_4Ce acted as a dispersant and hence reduced the dimensions of a single Fe-rich particle.

Besides, the formation of cerium-containing phase, e.g. Al_4Ce, Al_8FeCe_2, consumed the alloying elements for the formation of Al-Fe phases. Therefore, generally, the size of the Fe-rich needles and Chinese script tips was decreased after the addition of cerium. Since the addition of cerium also promoted more iron prccipitated, the absolute number of Fe-rich particles should increase, especially when their sizes were smaller. In addition, the cerium-containing phase also increased the particle densities in the Al alloy. Therefore, the total volume fraction of intermetallic phase should increase continually as

extra cerium was added.

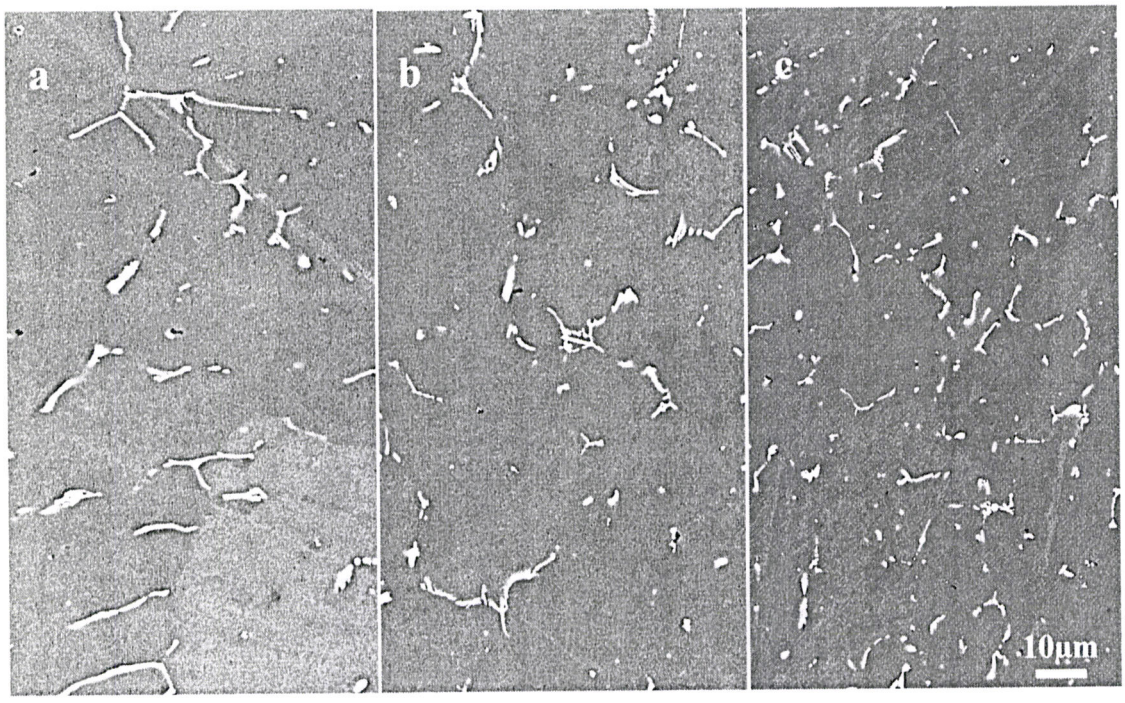

Figure 4.2 SEM micrographs of morphologies of intermetallics in AA5754 alloys at BSE mode: (a) Reference (b) 0.1 wt. % Ce contained alloy (c) 0.3 wt. % Ce contained alloys.

Therefore, after the size of the needles and Chinese script reduced, the stress concentration in the alloy would be partially released. Voids would not easily be initiated around them as before. Compared to the original geometry of the elongated Fe-rich particles, their present morphology was in aid of the formability of the alloys. It is still uncertain what morphology transformation mechanism it takes during the modification; some authorities declared that the absorption of cerium decreased this interfacial energy and hence retarded further growth of this particle. (Day, *et al.*,1964, D. Jaffrey *et al.*,

1969, Cline *et al.*, 1971). However, this morphology modification is achieved at the price of increasing volume fraction of intermetallic particles.

4.1.3 The Morphology and Volume Fraction of Intermetallics in 60% Reduction Alloys

Volume fraction of intermetallic particles is also a key factor to the formability of aluminum alloy. Following cold rolling, particles broke into small ones and formed in stringers at the L-ST plane, as seen in Figure 4.3. Since the resolution of this image analysis software, Eclipse 6.0, was less than 2 pixels (Northern Eclipse Help Reference Version 6.0), particles smaller than that would not be dissolved, which indicated a lower volume fraction measured than real values. Clusters of particles were observed in 0.3Ce alloy. This deformation imperfection could be diminished as the alloys were further rolled.

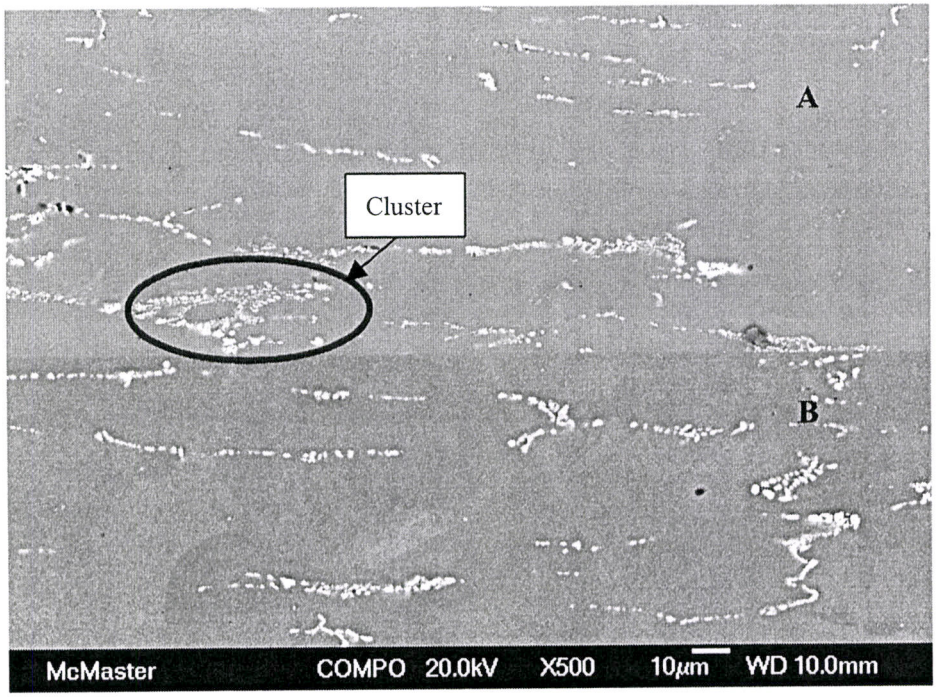

Figure 4.3 Stringers of Intermetallics formed 60% reduction AA5754 alloys (A) 0.3wt.% Ce (B) Reference

The images of the fine particles in 60% reduction alloy indicated that, the thermo-mechanical processing could eliminate the cerium effect on microstructure of the as-cast alloy. The intermetallic morphology and volume fraction would be even similar after 90% reduction deformation. Therefore, after thermo-mechanical processing, intermetallic phase morphology should have no significant influence on the reference and Ce-doped alloy.

4.1.4 Grain Refinement Mechanism

The grain microstructure was refined greatly by the addition of cerium. This is

due to the finely distributed Al_4Ce spheroids. In the Al-Mg-Fe alloy, like the Al-Fe intermetallics, Al_4Ce precipitated out at very high temperature at the very beginning of the solidification, even in the melt. They acted as heterogeneous nucleation sites for grains, and hence refined the grain structure of as-cast alloys. However, instead of increasing the number of such nucleation sites, further addition of cerium led to the formation of bigger cerium aluminides, which consumed the cerium for heterogeneous nucleation cites (as seen in Figure 4.4). Thus, no further grain refinement achieved in the 0.3Ce alloy.

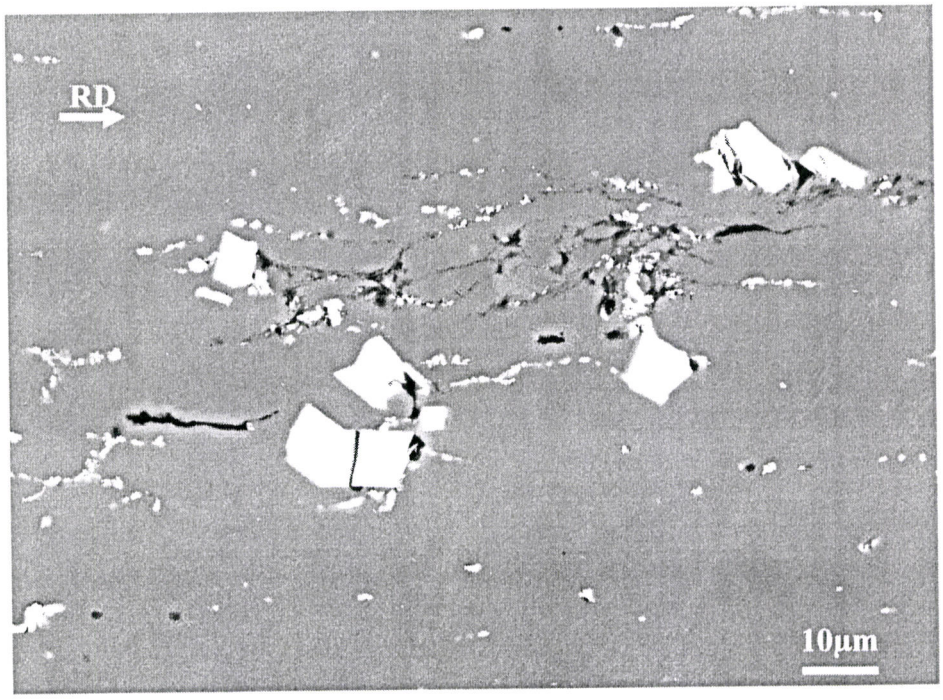

Figure 4.4 The plate-like cerium aluminide and severe local deformation around them in Al matrix of 60% reduction 0.3 wt. % cerium alloys.

However, this refinement effect would be eliminated when recrystallization completed during the thermomechanical processing in all three composition alloys. Since all alloys achieved similar grain microstructures, the difference of grain size was dramatically diminished, and even became negligible if further reduction was done.

4.2 The Non-heat-treatable Cerium-doped Al-Mg-Fe Alloys

Barth (1912) proposed that the addition of cerium would lead to precipitation hardening to aluminum alloys. The addition of erbium formed both primary Al_3Er and secondary Al_3Er in the Al-5Mg-0.4Er alloy, where extensive precipitations of secondary Al_3Er dispersoids enhanced the alloy strength and thus made the Al-Mg alloy a heat-treatable one (Xu G. *et al.*, 2006).

If the addition of cerium also formed such secondary precipitates that would also precipitate from supersaturated solid solution as Al_3Er did, the 0.3 Ce alloy should have much enhanced strength after artificial aging. However, the addition of cerium did not change the aluminum alloy into a heat-treatable alloy, and no secondary cerium-containing dispersoids formed during artificial aging. Although the mechanism was unknown, it could be predicted in the view of solubility and atomic radii. First of all,

the erbium might have higher solubility in Al matrix at high temperature than cerium. Secondly, with the bigger atomic number and smaller atom radius, erbium had more affinity with Al and hence it would be easier for Al_3Er dispersoids to precipitate from the Al matrix than the Al_3Mg_2. Third, as in Al-Mg-Fe alloy, the existence of Fe also decreased the solubility of cerium and that most of the cerium would precipitate at the very beginning of solidification, and hence not enough cerium could stay in the supersaturated solid solution and generate extensive precipitation hardening during aging.

The aging and hardness test proved this cerium-doped Al-Mg-Fe alloy remains non-heat-treatable. And it also confirmed the observation of Gillett and Schnee (1923) that no hardening effect appear due to the formation of any silicide.

4.3 Cerium Effect on the Mechanical Behavior of Al-Mg-Fe Alloy

4.3.1 Strengthening Effect

As discussed above, the increase in UTS of the as-cast alloys and thermo-processed alloys is mainly from the grain refinement. The addition of cerium provides grain refinement by acting as efficient heterogeneous nucleation cites and barriers to grain boundary movement. The deformed alloys completed fully

recrystallisation during annealing, and hence achieved refined grain structure and high strength. Due to the low solubility of cerium and small amount of addition, solid solution strengthening effect would not be obvious as that of magnesium in AA5754 alloys. Therefore, after cold working and annealing, the alloy of each composition got the similar grain microstructure and strength.

Although negligible decrease in UTS was observed in the 0.3Ce alloys, this slight decrease could be explained by the observation of few big cerium aluminide in the 0.3Ce alloys and the slight variation of grain sizes. This coarse aluminide particle would cause severe stress concentration in local Al matrix, and hence easily initiated void during deformation.

The material showed different mechanical behavior at RD and TD. This is due to the heterogeneous deformation during the rolling. The material has less deformation at TD than RD. Therefore, the specimens taken at TD would have larger grain sizes after recrystallisation than those at RD. And the strengthening effect was therefore less in transverse direction than that in rolling direction.

4.3.2 Prior Necking Behavior of Al-Mg-Fe Alloy

It was observed that neither the additions of cerium nor the thermo-mechanical processing had any effect on the uniform elongation of AA5754 alloys. Therefore, it is indicated that the prior-necking deformation process of AA5754 is not much influenced by the intermetallics and grain microstructures. This could be explained by the deformation mechanism of shear localization in AA5754 alloy. As Spencer *et al.* (2001) mentioned, it is a process of shear localization with a consequence of local damage only appeared at very late stage of the fracture process. Before that, the alloy just deformed homogenously. It was during the post necking period when voids were initiated around the coarse constituent particles and developed to produce final fracture along the localized shear bands.

4.3.3 Post Necking Behavior of Al-Mg-Fe Alloy

The post necking behavior of AA5754 alloy is a very short period on the profile of engineering stress-strain curves, as seen in Figure 4.5. Reduction in area at fracture surface was used for indicating the ductility and predicating bendability of the material. (by Datsko and Yang (1960)'s empirical equation).

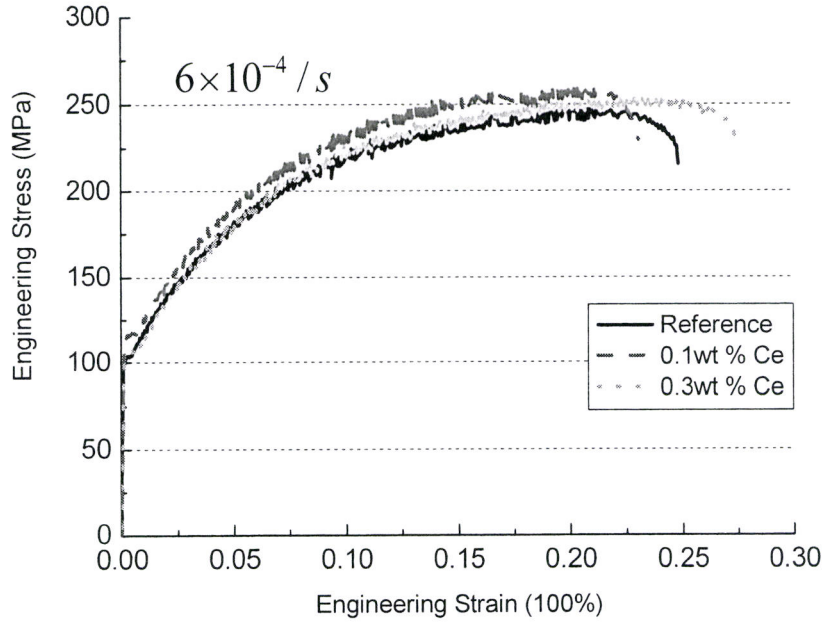

Figure 4.5 Engineering stress-strain curves of 60% cold rolled and annealed alloys

It was found out that, the further the alloy was deformed, the better ductility would be. Still, the addition of cerium has no measurable effect on alloy's ductility. This meant up to 0.3 wt.%, there were no effects of cerium additions on alloys' ductility and even bendability. As shown in Figure 4.6, it can be concluded that, the ductility and bendability were improved as grains were refined. Similar trend was observed for the specimens at TD. AA5754 sheet alloy had lower ductility at TD than at RD. This anisotropic ductility is also due to the difference in grain structure at RD and TD.

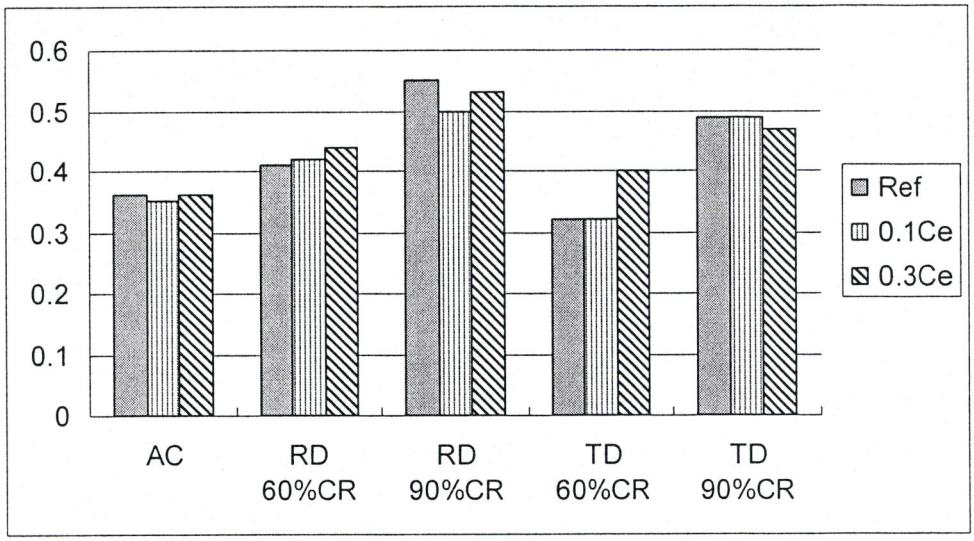

Figure 4.6 Reduction Areas of As-Cast and Rolled Specimens at RD and TD Directions

However, it was found that, from 60% reduction to 90% reduction alloys, their grain sizes varied little at L-ST plane, but an obvious increase in ductility was observed in 90% reduction alloy. This might be due to the refined grain structure at other planes. Grain refinement may be gained at planes, e.g. TD plane, through the further thermo-mechanical processing. The intermetallic particles and their distribution, which was different in 60% and 90% reduction alloy, may also attribute to this ductility enhancement. As Sarkar *et al.* (2001) mentioned, the fracture mechanism of Al-Mg-Fe alloy was influenced both by the shear localization and void initiation and linking along the shear bands. For the sheet alloy, the particles would be finer and formed in stringers in the 90% reduction alloy rather than coarse particle clusters in the 60% reduction alloy.

Therefore, the process of damage accumulation in t9he 90% reduction rolled alloy would be much slower than that in the 60% reduction rolled alloy, and a longer fracture strain would be achieved.

Cerium addition generated new phases and hence increased the intermetallic fraction in the alloys. The particle spacing was therefore decreased comparing to the reference alloy, especially in the as-cast ones. In this view, the addition of cerium should be detrimental to the alloy ductility because it might lead to fast void linking during the post necking period. However, from the view of the phase morphology, the newly appeared cerium-containing phase much favored the ductility of alloys comparing to the Fe-rich particles. In addition, it somehow modified the acicular Fe-rich particles by shortening their needle tips and breaking big particles. The two effects of the addition of cerium on the alloy intermetallics seemed to have canceled off each other, and resulted in a similar mechanical behavior in the as-cast alloys.

The advantage and disadvantage of the influence of cerium on the alloy microstructure would eventually cancel each other, and so the alloys of different composition did not behave differently in the tensile tests. However, this did not mean that addition of cerium had no modification effect on the alloy. If the iron content

accumulated to higher level, and more detrimental phase formed, e.g. when silicon content is higher, the modification effect of cerium on the alloy microstructure and mechanical property would be more obviously, then this small addition of chemicals might be commercial effective in alloy modification.

5 CONCLUSIONS

This project is focused on the effect of cerium additions on the microstructure and mechanical property of Al-Mg-Fe alloy. The alloys with modified compositions were fabricated and processed by lab-simulated die casting and thermo-mechanical processing. The microstructures were observed and the phases were identified by different quantification techniques. Macrohardness and Tensile Tests were conducted on alloy samples. The results and major achievements are summarized below.

1. Explored the effect of small additions of cerium on the formability of Al-Mg-Fe alloy. Determined that cerium is not be chosen as a modifier that can provide chemically-enhanced formability at small content level.

2. Proved the Al-Mg-Fe alloy with 0.1wt.% and 0.3wt.% Ce remains a non-heat-treatable alloy.

3. Discovered the existence of phases have not been reported in literature by XRD and TEM investigations of the reference and 0.3Ce alloys.

4. Explored the effect of small additions of cerium on the formability of Al-Mg-Fe

alloy. Determined that cerium is not be chosen as a modifier that can provide chemically-enhanced formability at small content level.

5. Proved the Al-Mg-Fe alloy with 0.1wt.% and 0.3wt.% Ce remains a non-heat-treatable alloy.

6. Discovered the existence of phases have not been reported in literature by XRD and TEM investigations of the reference and 0.3Ce alloys.

APPENDIX

1. Image Analysis (Northern Eclipse Version 6.0 Help Reference, Empix Imaging, Inc., 2001.)

The total number of pixels that an object occupies is measured as its area. After calibration, the area of the selected objects can be attained. The volume fraction of selected objects can be therefore calculated upon the statistical data of the area fraction.

Shape Factor of an object is defined as $(4\times\pi\times Area)/(Perimeter^2)$. This gives an indication as to the objects shape. Circles have the greatest area to perimeter ratio and this formular will approach a value of 1 for a perfect circle. A thin thread-like object would have the lowest shape factor approaching 0. The value of shape factor is in a inverse relationship with aspect ratio. Therefore, the higher the shape factor of a particle, the lower aspect ratio it will have.

2. Young's equation (Datsko J. and Yang CT., J. Engg. Industry 82 (1960))

$\frac{r_{\min}}{t}=\frac{C}{RA}-1$, where C is a constant, r_{min} is the minimum radius without fracture when bended, t is the thickness of the sheet alloy. RA is the reduction in area, which indicate the ductility of the material. Since the left side of the equation stands for the bendability of the alloy, the alloy bendability can be related to its ductility by RA.

3. Phase Diagram

Al-Mg-Fe Ternary Phase Diagram (Landolt Bornstein IV 5a, pp285)

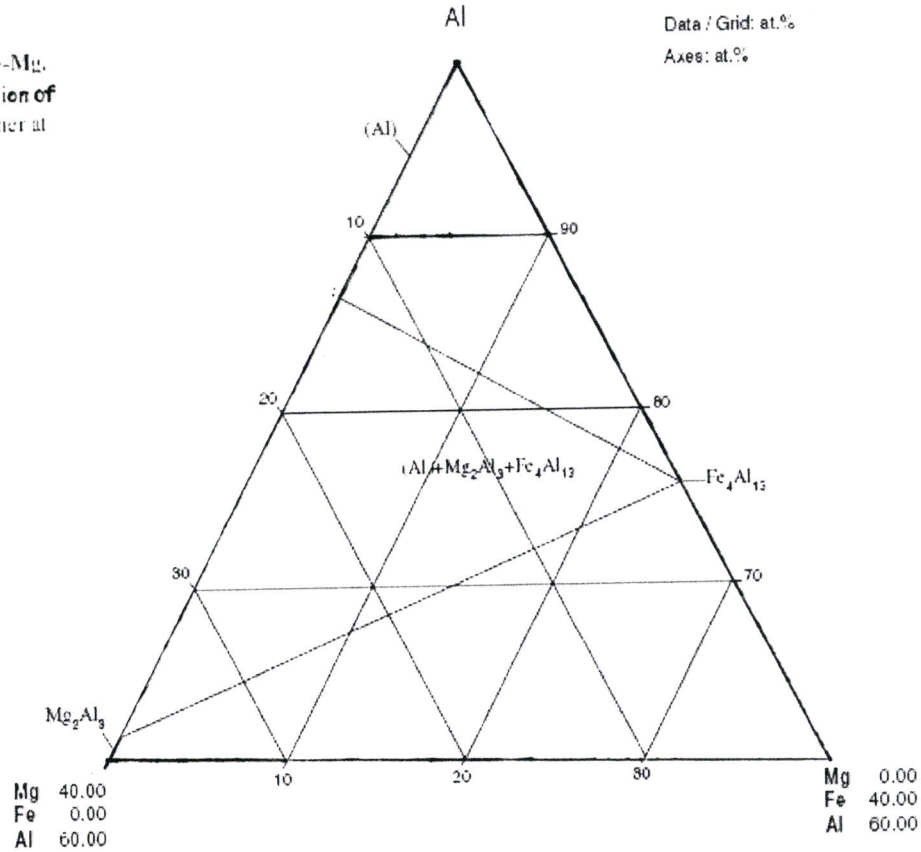

Fig. 4: Al-Fe-Mg. Isothermal section of the Al-rich corner at 400°C

Al-Ce-Fe Ternary Phase Diagram (Landolt Bornstein IV 5a, pp196)

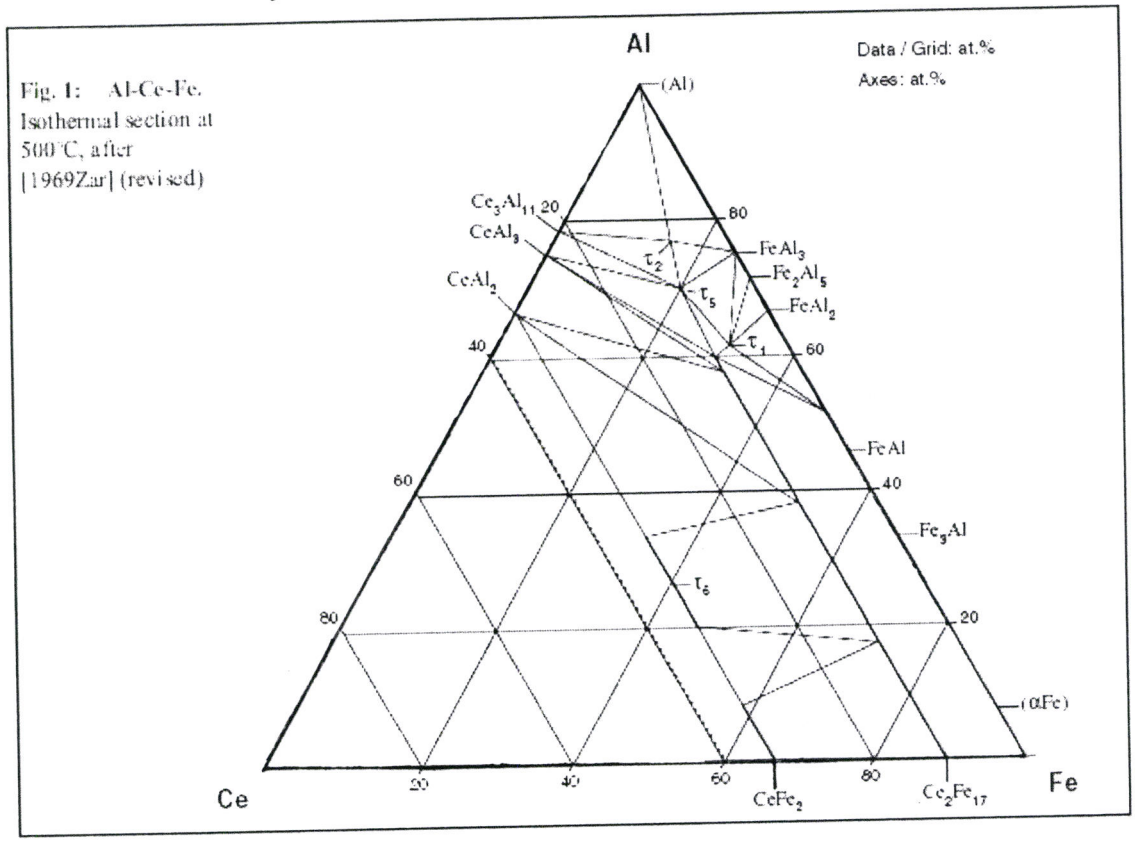

Fig. 1: Al-Ce-Fe. Isothermal section at 500°C, after [1969Zar] (revised)

* τ_1, $CeFe_4Al_8$	*tI26*	*a* 886	[1961Gla]
	I4/mmm	*c* 508	
	$ThMn_{12}$	*a* 880.5	[1976Bus]
		c 504.8	
* τ_2, $CeFe_2Al_{10}$	*oC52*	*a* 900.02	[1998Thi]
	Cmcm	*b* 1022.2	
	$YbFe_2Al_{10}$	*c* 907.3	
* τ_3, $Ce_6Fe_{11}Al_3$		*a* 819.03	[1992Hu]
		c 2310.08	
* τ_4, $CeFe_2Al_8$	*oP44*	*a* 1251	[1974Yar]
		b 1448	
	$CeFe_2Al_8$	*c* 407	

REFERENCE

Asensio-Lozano J, *Suarez-Pena B, Scripta Materialia* **54** 5(2006) 943-947.

ASM Handbook Vol.**8**, *Mechanical Testing and Evaluation*, **10**th edition (2000) ASM International.

ASM Handbook Vol.**9**, *Metallography and microstructures*, **10**th edition (2004) ASM International .

ASM Handbook, Vol. **3**, *Alloy Phase Diagram,* ***2nd*** *edition (1992)* ASM International.

ASM Handbook, Vol.**2**, *Properties and Selection: Nonferrous alloy and special-purpose materials*, 10th edition (1991) ASM International.

Ayer R, Angers LM, Mueller RR, Scanlon JC, Klein CF, *Metallurgical and materials transactions* **19**A (1998)1645-1656.

Azari HN, Girard SX, Wilkinson DS, Lloyd DJ, *Metallurgical and materials transactions* **35** A (2004) 1839-1851.

Bakke P, Westengen H, *JOM* **56** n11 (2004) 191.

Barth, *Metallurgie.* **8** (1912) 261.

Brown LM, Embury JD, *Institute of Metals, London, Monograph and Report Series*, 1973.

Buschow, KHJ, Vucht V, Hoogenhof JHN, *J. Less-Common Met.* **50** (1976) 145-150.

Cai W, Xu M, Lax Melvin, Alfano R R, *Optical Letters* **27** n 9 (2002) 731-733.

Chen Y, Fu G, Li Y, Chen W, *Special casting and nonferrous alloys* **26** (2006) 22-25.

Datsko J, Yang CT, *Journal of Engineering Industry* **82** (1960) 309.

Dieter GE, *Mechanical Metallurgy*, 3rd edtion, McGraw-Hill Inc. (1986).

Friedman PA, and Sherman AM, *Proceeding of the Symposium on Automotive Alloys, TMS* **32** (1998)147-160.

Gillett HW and Schnee VH, *Industrial and Engineering Chemistry* (1923) 709.

Girard S, *Efffect of thermomechanical processing on texture development in a twin-belt cast automotive aluminum alloy*, Mcmaster University, master thesis (2002).

Griger A, Stefaniay V, *Journal of materials science* **31** (1996) 6645-6652.

Grobner J, Kevorkov D, Schmid-Fetzer R, *Intermetallics* **10** 5 (2002) 415-422.

Gschneidner K, Russell A., Pecharsky, Alxandra *Nature Materials* **2** (2003) 587-590.

Gupta AK, Marois PH, Lloyd DJ, *Materials Characterization* **37** (1996) 61-80.

Hirsch, Trans. Am. *Electroche*m. *Soc.* **20** (1911) 57.

Kang J, Wilkinson DS, Jain M, Embury JD, Beaudoin AJ, Kim S, Mishira R, Sachdev AK, *Acta Meterialia* **54** (2006) 209-218.

Kang JD, Wilkinson DS, Embury JD, Hussain K, *Materials Science Forum* **519-521** (2006) 985-990.

Kang JD, Wilkinson DS, Malakhov DV, Halim H, Jain M, Embury JD, Mishra RK, *Materials Science and Engineering A* **456** (2007) 85-92.

Khudokormov DN, Galushko AM, Lekakh SN, *Russ Cast Prod* **5** (1975) 198-199.

Kim YG., Farouk B, Apelian D, *Modeling of Casting and Welding Processes,* (1988) 265-274

Kosuge H, Takada H, *J. Japan Inst. Light Met.* **29** (1979) 64-69.

Korbel A, *Acta Metall.* **34** (1986) 1999.

Korbel A, Bochniak W, *Scripta Materialia*, **51** n8 (2004) 755-759.

Li Y, Olsen A, *JOM* **56** 11 (2004) 3.

Li Z, Bian X, Han X, Sun B, *Journal of casting technology* **11**, 2006 1210-1213.

Liang D and Jones H, *Materials Science and Engineering A***173** (1-2) (1993) 109-114.

Lolyd DJ, *Metallurgical and materials transactions* **11**A (1980) 1287.

Metals Handbook, Vol.**2**, *Properties and Selection: Nonferrous alloy and special-purpose materials*, **10**th edition, (1990) ASM International.

Mohamed K, Khatwa A, Malakhov DV, *Computer Coupling of Phase Diagrams and Thermochemistry* **30** (2006) 159-170.

Mondolfo LF, *Aluminum Alloys: Structure and Properties,* edition (1976) Butter Workth.

Morris DG, Munoz-Morris MA., Acta Materialia 50 (2002) 4047-4060

Okamoto H J, *Phase Equilibria* **19** (1998) 396.

Petry CJ, *Aluminum Alloys-Their Physical and Mechanical Properties, international*

conference at the University of Virginia, Charlottesville, Virginia, (1986)15-20.

Ravi M, Pillai UTS, Pai BC, Damodaran AD, Dwarakadasa ES, *Metallurgical and Materials Transactions A* **27A** 1283-92.

Ravi M, Pillai UTS, Pai BC, Damodaran AD, Dwarakadasa ES, *Metallurgical and Materials Transactions A* **33A** (2002) 391.

Rokhlin L, Bochvar NR, Lysova EV, and Dobtkina TV, *Metal Science and Heat Treatment* **46** 3-4 (2004) 106-109.

Saccone A, Cacciamani G, Maccio D, Borzone G, Ferro R, *Intermetallics* **6** (1997) 201-215.

Salazar M, Perez R, Rosas G, *Materials Science Forum* **426-432** 3 (2003) 1837-1842.

Sarkar J, Kutty TRG, Conlon KT, Wilkinson DS, Embury JD, Lloyd DJ, *Materials Science and Engineering A* **316** (2001) 52-59.

Schulte, Metall U. Erz, 18 (1921), 236. *Translation with comments by "R.E. Search" in Metal Ind.* **20** (1921) 142.

Sikora E, Shaw BA, Sharma-Judd M, *Proceedings of the International Symposium*, (2005) 244-255.

Spencer K, Corbin SF, Lloyd DJ, *Materials Science and Engineering A* **332** (2001) 81-90.

Spencer K, Corbin SF, Lloyd DJ, *Materials Science and Engineering A* **325** (2002) 394-404.

Suarez-Pena B, Asensio-Lozano J, *Scripta Materialia* **54** (2006) 1543-1548.

Sun W, *The Effect of Rare-earth element on Aluminum Alloys,* 1st edition (1992), Bingqi Press.

Tang D, Wang L, Zhao M, *The Chinese Journal of Rare-Earth*, **10** (1) (1992) 66-71.

Teirlinck D, *Acta Metall.* **36** (1988) 1213.

Thiede VMT., Ebel T, Jeitschko W, *Journal of Materials Chemistry* **8** (1) (1998) 125-130.

Xu G, Yang J, Jin T, Nie Z, Yin Z, *The Chinese Journal of Nonferrous Metals*, **16** 5 (2006) 5.

Yarmolyul, Ya P, Rykhal RM, Zarechnyuk O.S., Tezisy Dokl. Vses. *Kong. Kristallokhim, Rykhal, R.M ed. Intermetalicheskie Soedineniya,* **2**nd edition, (1974) 39-40.